Acta Geologica Sinica (English Edition), 2019, 93(2): 265–282

The Late Carboniferous–Early Permian Ocean-Continent Transition in the West Junggar, Central Asian Orogenic Belt: Constraints from Columnar Jointed Rhyolite

XU Shenglin[1, 2], CHEN Xuanhua[2, *], LI Tingdong[1, 2], SHI Jianjie[2], DING Weicui[2], LI Bing[2], HUANG Penghui[2, 3], ZHANG Yiping[2], ZHANG Yaoyao[2] and MA Feizhou[2]

[1] *School of Earth Sciences and Resources, China University of Geosciences, Beijing 100083, China*
[2] *Chinese Academy of Geological Sciences, Beijing 100037, China*
[3] *Beijing Research Institute of Geological Engineering Design, Beijing 101500, China*

Abstract: The West Junggar of the western Central Asian Orogenic Belt is one of the typical regions in the term of ocean subduction, contraction and continental growth in the Late Paleozoic. However, it is still controversial on the exact time of ocean-continent transition so far. This study investigates rhyolites with columnar joint in the West Junggar for the first time. Based on zircon U-Pb dating, we determined that the ages of the newly-discovered rhyolites are between 303.6 and 294.5 Ma, belonging to Late Carboniferous–Early Permian, which is the oldest rhyolite with columnar joint preserved in the world at present. Geochemical results show that the characteristics of the major element compositions include a high content of SiO_2 (75.78–79.20 wt%) and a moderate content of Al_2O_3 (12.21–13.19 wt%). The total alkali content (K_2O + Na_2O) is 6.14–8.05 wt%, among which K_2O is 2.09–4.72 wt% and the rate of K_2O/Na_2O is 0.38–3.05. Over-based minerals such as Ne, Lc, and Ac do not appear. The contents of TiO_2 (0.09–0.24 wt%), CaO (0.15–0.99 wt%) and MgO (0.06–0.18 wt%) are low. A/CNK=0.91–1.68, A/NK=1.06–1.76, and as such, these are associated with the quasi-aluminum-weak peraluminous high potassium calc-alkaline and some calc-alkaline magma series. These rhyolites show a significant negative Eu anomaly with relative enrichment of LREE and LILE (Rb, Ba, Th, U, K) and depletion of Sr, HREE and HFSE (Nb, Ta, Ti, P). These rhyolites also have the characteristics of an A2-type granite, similar to the Miaoergou batholith, which indicates they both were affected by post-orogenic extension. Combining petrological, zircon U-Pb dating and geochemical characteristics of the rhyolites, we conclude that the specific time of ocean-continent transition of the West Junggar is the Late Carboniferous–Early Permian.

Key words: rhyolite, columnar joint, zircon U-Pb dating, geochemistry, ocean-continent transition, West Junggar

Citation: Xu et al., 2019. The Late Carboniferous–Early Permian Ocean-Continent Transition in the West Junggar, Central Asian Orogenic Belt: Constraints from Columnar Jointed Rhyolite. *Acta Geologica Sinica* (English Edition), 93(2): 265–282. DOI: 10.1111/1755-6724.13812

1 Introduction

The Central Asian Orogenic Belt (CAOB) is a giant suture zone between the Tarim–North China craton, the European craton and the Siberian craton (Fig. 1; Feng et al., 1989; Sengör et al., 1993; Xiao et al., 2012). It was formed during the colusion of the Paleo-Asian Ocean and is the most significant orogenic belt (Xiao and Kusky 2009; Li Wei et al., 2010; Chen et al., 2015; Jin et al., 2015; Liu et al., 2018). The tectonic–magmatic activity of the CAOB was very complex during the Paleozoic: it first formed a continental basement, which then underwent Paleo-Asian Oceanic subduction and continental margin accretion, followed by uplift and subduction of intracontinental fault blocks (Yakubchuk 2004,2008; Chen et al., 2009, 2011; Huang et al., 2016; Yu et al., 2018). Multi-stage and variable rocks were developed in the CAOB, including ultrabasic rocks, basic rocks, granite and volcanic rocks (Zhang et al., 2017; Ai et al., 2018; Sun et al., 2018).

The West Junggar is located in the western part of the CAOB (Fig. 1), a key location in the subduction, accretion and ocean-continent transition between the Kazakhstan micro-plate and the Junggar Ocean (Windley et al., 2007; Zhao et al., 2013; Li et al., 2017b). The vertical and lateral accretion of continental crust is significant with complex and diverse tectonic deformation in this area (Shen et al., 2013b; Chen et al., 2015; Zhan et al., 2015). The West Junggar is one of the most prominent regions that record the Late Paleozoic ocean-continent transition, which caused the development of a series of magmatic rocks. In addition, this area also hosts well-developed mineral resources and complex tectonic, which is an important tectonic–magmatic–metallogenic belt in the CAOB (Xiao et al., 2008; Chen et al., 2011; Shen et al., 2012; Yang et al., 2012; Shen et al., 2013a; Chen et al., 2014; Yang Yi et al., 2015).

Previous researchers have conducted a large number of chronological and geochemical studies and provided many results on the Late Paleozoic granite about the West Junggar. Han et al. (2006) suggested that the West Junggar Ocean basin closed before the Late Carboniferous and entered the post-collision stage during the Late

* Corresponding author. E-mail: xhchen@cags.ac.cn

http://www.geojournals.cn/dzxbcn/ch/index.aspx; https://onlinelibrary.wiley.com/journal/17556724

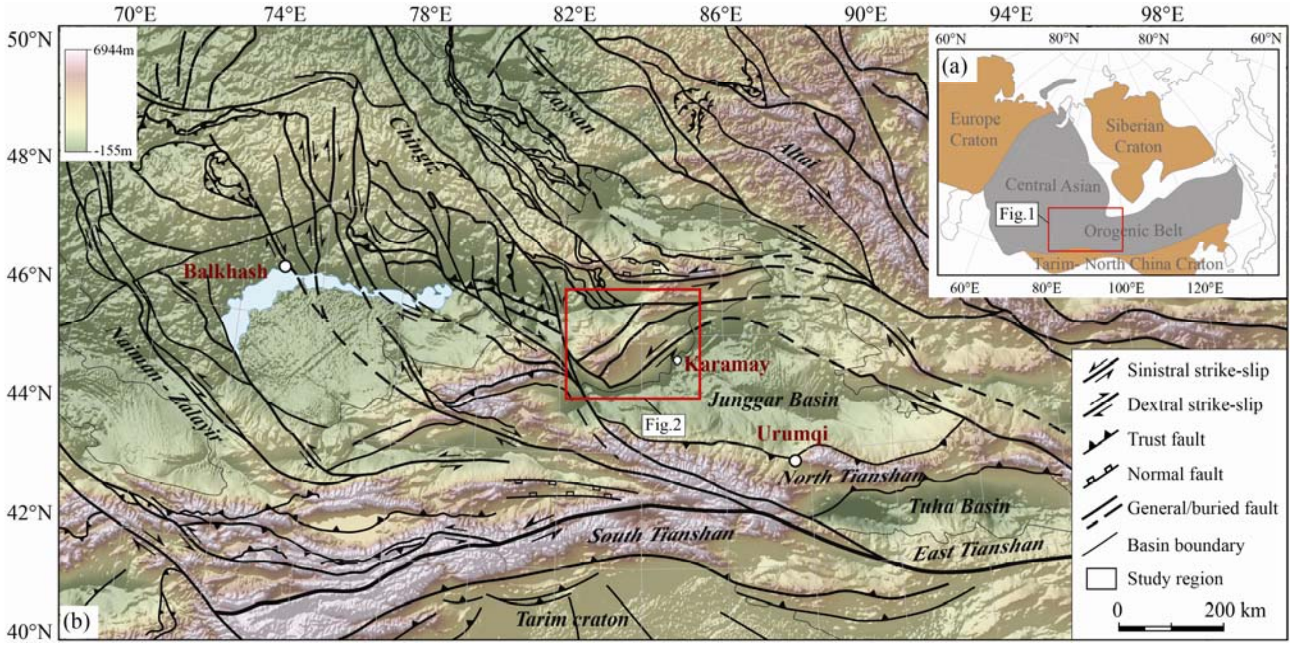

Fig. 1. (a) Simplified tectonic sketch of the Central Asian Orogenic Belt (modified from Jahn, 2004; Han et al., 2010). (b) tectonic setting in the western part of the Central Asian Orogenic Belt (modified from Buslov et al., 2004; Li et al., 2007; Chen et al., 2014; Li et al., 2017c).

Carboniferous–Permian (340–275 Ma). Tang et al. (2009) suggested that oceanic subduction in the West Junggar had not finished during the Late Carboniferous. Liu et al. (2009) suggested that this area still included an oceanic basin at 302 Ma. Additionally, Tang et al. (2010a, 2010b) suggested the existence of a Carboniferous oceanic ridge subduction or slab window tectonic environment. They have proposed numerous interpretations in the term of tectonic environment. However, their views regarding oceanic plate subduction polarity and the time limits of ocean-continent transition remain controversial. When did the West Junggar Ocean close? Generally, discriminating post-orogenic extension environment represented by magmatic rocks could be one of the great methods about ocean-continent transitional tectonic environment. But beyond that, is there any other significant feature that can be used as evidence for ocean-continent transition of the Western Junggar area?

We discovered new exposures of rhyolites with columnar joint near the Miaoergou batholith of the West Junggar. Based on its petrological, zircon U-Pb dating, petrogeochemical characteristics and a comparison to rhyolites with columnar joint from the western Pacific area, this paper provides new evidence for exploring the tectonic evolution of the West Junggar in the Late Paleozoic.

2 Geological Setting

The West Junggar is the northern branch of the eastern extension of the Devonian–Carboniferous residual oceanic basin in the Balkhash Basin, which contains Paleozoic sedimentary units that are mostly Devonian and Carboniferous (Fig. 2). The Paleozoic can be divided into two tectonic units: (1) an Early Paleozoic metamorphic terrain, which mainly consists of ophiolitic melange and flysch formation that show intense ductile shear deformation and metamorphism; and (2) a thick, Late Paleozoic, marine terrigenous clastic–volcaniclastic sedimentary formation (Chen et al., 2011; Tao et al., 2013; Zhu et al., 2013; Ma et al., 2017).The Carboniferous can be divided into the lower Carboniferous (C_1) and upper Carboniferous (C_2), which is characterized by thick volcanic–clastic rocks of bathyal–continental slope facies (Zhang et al., 2011). The lower Carboniferous (C_1), consisting of tuff, tuffaceous siltstone, siliceous rock and tuffaceous pebbly sandstone, is divided into Xibeikulasi Formation (C_1xb), Baogutu Formation (C_1b) and Tailegula Formation (C_1t) (Zhang et al., 2011; Chen et al., 2015). The upper Carboniferous (C_2), consisting of andesitic porphyrite, tuff, tuffaceous sandstone, glutenite, arkose, basalt and siliceous rock, is divided into Molaoba Formation (C_2m), Kujiertai Formation (C_2k) and Chengjisihanshan Formation (C_2c).

The West Junggar is the eastern extension of the Balkash Orogenic Belt (Fig. 1), which is surrounded by Chingiz–Junggar fault, Ertix strike-slip fault and Tianshan Orogenic Belt and is in the core area of the western CAOB (Laurent-Charvet et al., 2002).The tectonic orientation of the western CAOB is in the NW direction, whereas the West Junggar contains a NE-strike-slip fault system, along which a series of granitic exposures of different sizes have developed (Fig. 2, Chen et al., 2015; Huang et al., 2016).

The magmatic rocks comprised of acidic-ultrabasic rocks are widely distributed in the West Junggar (Li et al., 2017a; Yin et al., 2018). The most exposed magmatic rocks are granites, then ultrabasic rocks, and the basic rocks are only sporadic distributed (Song et al., 2007).Miaoergou batholith, surrounded by Darabut fault, Anqi fault and Mayile fault, is one of the largest batholiths

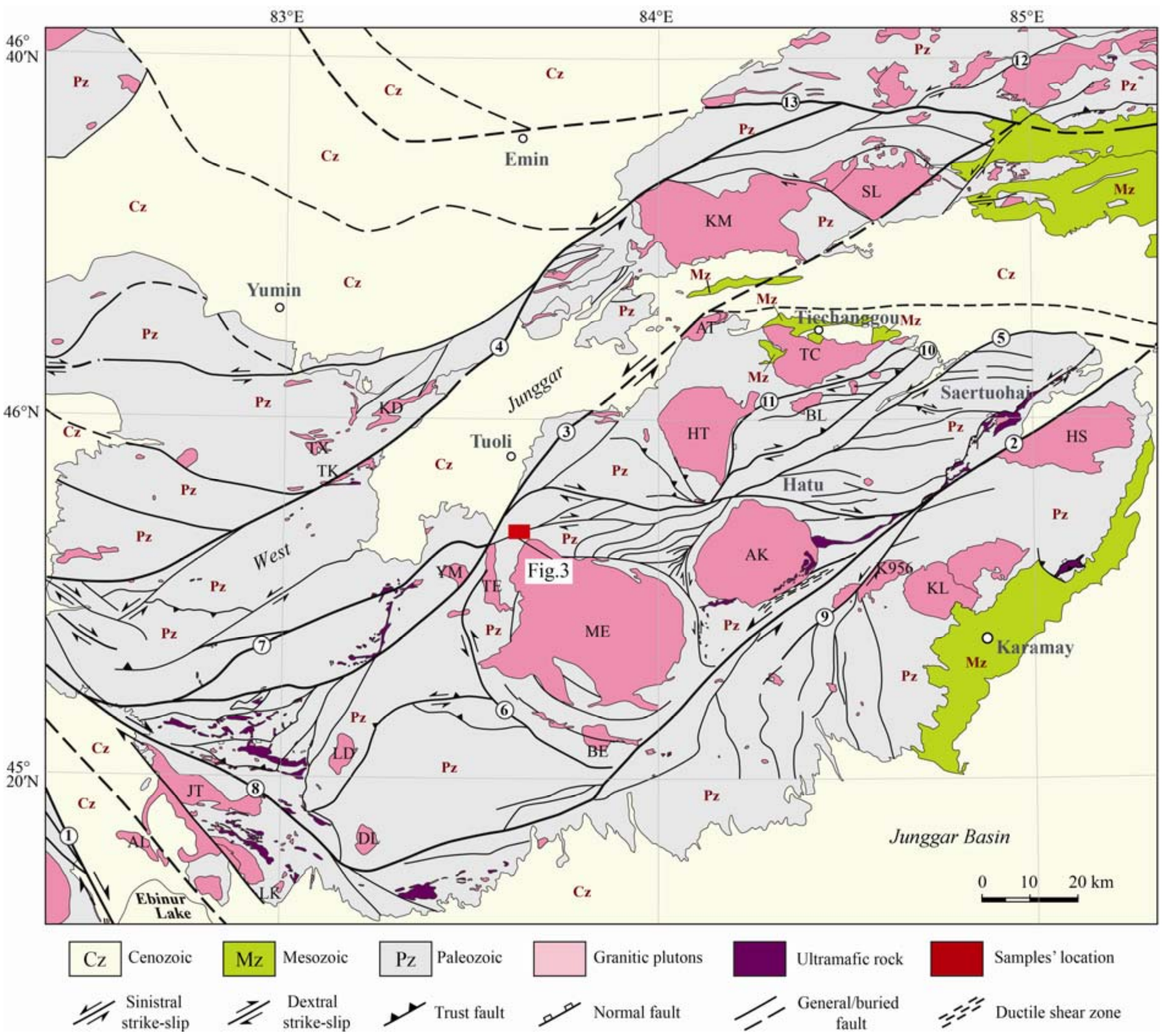

Fig. 2. Map of fault system and sample locations within the West Junggar (modified from Chen et al., 2011, 2015; Huang et al., 2016; Li et al., 2017c).

1, Chingiz–Junggar fault; 2, Darabut fault; 3, Mayile fault; 4, Baerluke fault; 5, Anqi fault; 6, Targen fault; 7, Mayatu fault; 8, Zhalouleshan–Balashan fault; 9, Yijiaren fault; 10, Hatu fault; 11, Bieluagaxi fault; 12, Xiemistay fault; 13, Yangzhuang fault. AK, Aketiereke pluton; AL, Alashakou pluton; BE, Buerkesitai pluton; BI, Baogutu pluton; BL, Bieluagaxi pluton; DL, Dulunhedong pluton; GZ, Gezidong pluton; HT, Hatu pluton; HS, Hongshan pluton; JT, Jietebutiao pluton; K956, K956 pluton; KD, Kangde pluton; KL, Karemay pluton; KM, Kulumusu pluton; LD, Labahedong pluton; LK, Labahekou pluton; ME, Miaoergou batholith; SL, Sailike pluton; TE, Targen pluton; TK, Takergan pluton; YM, Yamatu pluton; YY, Yuyi pluton.

in the area(Fig. 2) and is mainly A-type alkali-feldspathic granite(Han et al., 2006; Su et al., 2006; Zhou et al., 2008).Previous researchers have considered Miaoergou batholith may have yielded from post-collisional magmatism (Han et al., 2006; Su et al., 2006; Chen et al., 2010; Li et al., 2013).

3 Petrography

3.1 Field observations

The rhyolites with columnar joint were collected from the northwestern side of the Miaoergou batholith in the West Junggar (Fig. 2).The rhyolites with columnar joint belong to upper Carboniferous Chengjisihanshan Formation (C_2c) in the stratigraphic sequence, lying above lower Carboniferous Baogutu Formation marine terrigenous clastic–volcaniclastic assemblage and surrounded by C_2c in the field (Fig. 3). A total of six rhyolite samples were collected (sampling location is given in Fig. 3).

The columnar joint of rhyolite, with an average pillar length greater than 5 m, is a kind of primary structure (Fig. 4–a, b). The joints are tetragonal, pentagonal and hexagonal columnar joints that are dominated by hexagonal columns. The rhyolite in cross-section is a slightly flattened polygon (Fig. 4–c, d). Statistical results show that the major and minor axes of the cross-section are 26 cm and 23 cm for the tetragonal column, 28–34 cm and 25–26 cm for the pentagonal column and 37–47 cm and 27–38 cm for the hexagonal column. The attitude of the rhyolite bedding is at dip direction of 121°–141° with dip angle of 52°–65°; the plunge attitude of columnar rhyolite is 257°–275° with a plunge angle of 21°–32°. The

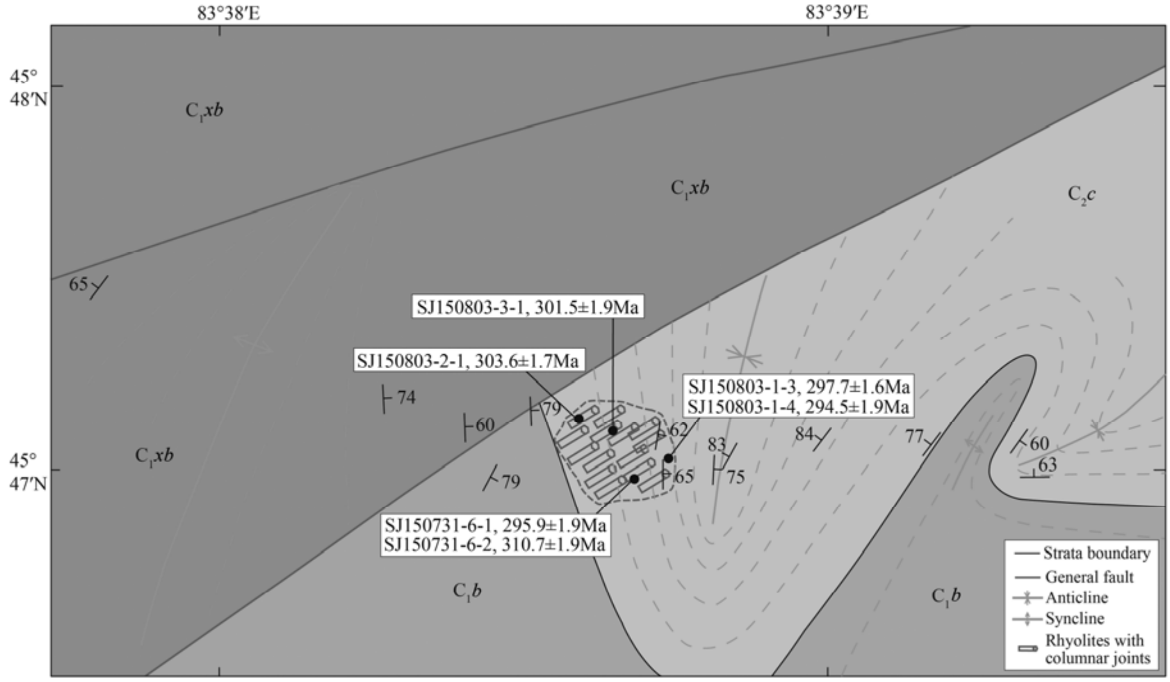

Fig. 3. Sketched geological structure map of columnar jointed rhyolites.
C_2c, Upper Carboniferous Chengjisihanshan Formation; C_1b, Lower Carboniferous Baogutu Formation; C_1xb, Lower Carboniferous Xibeikulasi Formation.

orientation of rhyolite columns is generally perpendicular to the rhyolite bedding plane.

3.2 Petrographical characteristics

Rhyolite samples SJ150731-6-1, SJ150731-6-2, SJ150803-1-3 and SJ150803-1-4 have similar microstructures, including porphyritic textures with felsitic–microlitic matrix and an underdeveloped rhyolitic structure. The phenocrysts mainly consist of quartz and alkaline feldspar with sporadic plagioclase, and the matrix is mainly feldspar, quartz and mica. The volume fraction of phenocrysts is 20%–30%, among which quartz is semi-euhedral with grain size of 0.5–2.5 mm and accounts for 50% of the phenocryst volume fraction. The alkaline feldspar crystals are euhedral, long-columnar to short-columnar, with visible cassette twins and a column length of 0.5–1.0 mm, and account for 45% of the phenocryst volume fraction. Mica accounts for 5 % (Fig. 5a–d). Sample SJ150803-2-1 has a porphyritic texture with a rhyolitic structure and an aplitic matrix. Its phenocrysts are dominated by feldspar and quartz, with a volume fraction of 15%–25% and a grain size of 0.2–0.5 mm (Fig. 5e). Sample SJ150803-3-1 has a mainly spherulitic texture with approximately 90% spherulitic aggregates with diameters of 0.5–1 mm. It mainly consists of feldspar and quartz (Fig. 5f).

4 Petrogeochemistry

4.1 Method

Chemical analyses of the rhyolite were performed at the National Research Center for Geoanalys, Chinese Academy of Geological Sciences. Samples were ground to below 200 mesh. Except FeO, the detection of major elements uses standard GB/T14506.28–1993, and the detection of FeO uses standard GB/T14506.14–1993. The detection of H_2O^+, CO_2 and the loss on ignition (LOI) uses standards GB/T14506.2–1993, GB9835–1988 and LY/T1253–1999, respectively. Except FeO, which is determined by the volumetric titration method, all other major elements are determined by X-ray fluorescence spectrometry (XRF). The detection of trace elements and rare earth elements uses standard DZ/T0223–2001, an acid melting method and Excel-type ICP-MS.

4.2 Results

The analytical results of the main elements and trace elements of the rhyolite samples are given in Tables 1 and 2. Results show that the characteristics of the major element compositions include a high content of SiO_2 (75.78–79.20 wt%) and a moderate content of Al_2O_3 (12.21–13.19 wt%). The total alkali content (K_2O+Na_2O) is 6.14–8.05 wt%, among which K_2O is 2.09–4.72 wt% and the rate of K_2O/Na_2O is 0.38–3.05. Over-based minerals such as Ne, Lc, and Ac do not appear. The contents of TiO_2 (0.09–0.24 wt%), CaO (0.15–0.99 wt%) and MgO (0.06–0.18 wt%) are low.

The six rhyolite samples are all located in the rhyolite zone in the igneous rock TAS (Total Alkali versus Silica) classification diagram (Fig. 6a) with A/CNK (Al_2O_3/(CaO+Na_2O+K_2O), molratio)=1.05–1.68 and A/NK (Al_2O_3/(Na_2O+K_2O), molratio)=1.08–1.75. The projection of A/CNK-A/NK in the diagram mostly plot into the quasi -aluminum weak peraluminous zone, which is generally consistent with the Miaoergou batholith (Huang et al., 2016) (Fig. 6b). This suggests that the samples are from the mainly high-potassium calc-alkaline series, with a few from the calc-alkaline series (Fig. 6c, d), which is

Fig. 4. Outcrop photos of columnar jointed rhyolites.

Table 1 Major element compositions (wt%) of rhyolites from the Western Junggar

Sample number	SiO_2	TiO_2	Al_2O_3	Fe_2O_3	FeO	MnO	MgO	CaO	Na_2O	K_2O	P_2O_5	H_2O^+	CO_2	LOI	Total
SJ150731-6-1	77.37	0.09	12.89	0.57	0.32	0.18	0.04	0.19	1.48	4.52	0.04	1.62	0.33	1.62	101.26
SJ150731-6-2	75.41	0.11	12.49	0.79	0.47	0.10	0.01	0.97	3.08	4.63	0.03	0.78	0.5	1.37	100.74
SJ150803-1-3	75.94	0.09	12.28	0.88	0.54	0.11	0.01	0.57	3.05	4.47	0.03	0.84	0.5	1.26	100.57
SJ150803-1-4	74.42	0.10	12.56	1.20	0.25	0.09	0.01	1.20	2.97	4.51	0.04	0.96	1.13	1.74	101.18
SJ150803-2-1	74.45	0.24	12.35	2.84	0.18	0.06	0.05	0.15	5.04	2.87	0.02	0.58	0.5	0.59	99.92
SJ150803-3-1	77.21	0.20	12.09	1.46	0.25	0.06	0.02	0.19	5.42	2.07	0.03	0.44	0.33	0.49	100.26

Table 2 Trace element compositions (ppm) of rhyolites from the Western Junggar

Sample number	La	Ce	Pr	Nd	Sm	Eu	Gd	Tb	Dy	Ho	Er	Tm	Yb
SJ150731-6-1	25.1	61.5	8.63	35.4	9.39	0.17	10.0	1.8	12.2	2.65	7.32	1.07	6.64
SJ150731-6-2	21.0	51.9	6.71	28.8	6.98	0.17	6.83	1.23	8.10	1.68	4.83	0.70	4.54
SJ150803-1-3	24.2	58.9	7.97	32.9	8.19	0.16	8.24	1.48	9.66	2.07	5.70	0.83	4.95
SJ150803-1-4	24.4	59.3	8.09	33.0	8.28	0.18	8.44	1.54	9.98	2.08	6.22	0.89	5.47
SJ150803-2-1	32.6	58.5	9.78	41.4	9.70	1.72	9.27	1.48	9.24	1.91	5.33	0.80	5.31
SJ150803-3-1	27.9	60.3	8.31	37.0	8.30	1.11	8.26	1.37	9.02	1.87	5.40	0.80	5.11

Sample number	Lu	Y	Rb	Ba	Th	U	Nb	Ta	Pb	Sr	Zr	Hf	Ga
SJ150731-6-1	0.99	69.2	138	257	12.1	3.08	6.23	0.63	9.43	24.3	100	4.41	22.3
SJ150731-6-2	0.67	43.7	106	207	9.55	2.15	6.27	0.64	12.00	32.5	91.3	4.12	19.2
SJ150803-1-3	0.72	51.6	103	201	11.3	2.41	6.30	0.59	9.44	33.2	94.2	4.15	19.7
SJ150803-1-4	0.81	55.9	106	196	11.2	2.27	6.47	0.57	18.40	46.7	99.2	4.30	20.4
SJ150803-2-1	0.81	49.4	63.9	871	6.41	2.50	8.95	0.65	7.46	33.9	344	11.1	18.7
SJ150803-3-1	0.74	46.3	53.3	542	7.66	2.48	9.26	0.64	6.41	42.7	355	11.6	17.8

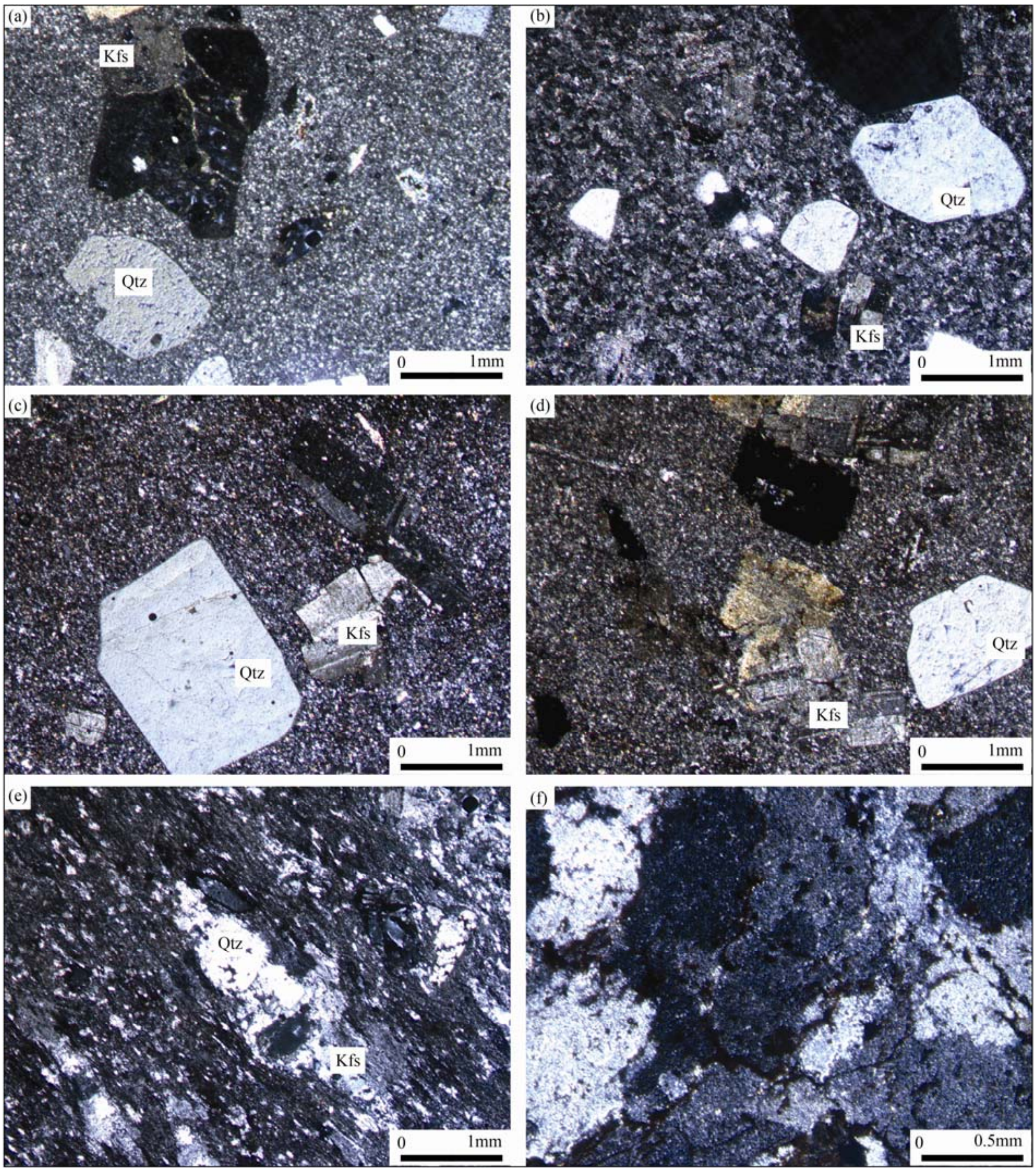

Fig. 5. Microstructures of rhyolite samples.

(a) sample SJ150731-6-1; (b) sample SJ150731-6-2; (c) sample SJ150803-1-3; (d) sample SJ150803-1-4; (e) sample SJ150803-2-1; (f) sample SJ150803-3-1. Qtz, quartz;Kfs, potash feldspar.

generally consistent with the Miaoergou batholith (Huang et al., 2016). Except for Na_2O and K_2O, the major elements of the rhyolite samples and the closest sample from the Miaoergou batholith are negatively correlated with SiO_2 (Fig. 7). Rhyolite is located at the end of magmatic differentiation, suggesting that it may share its magma origin with the Miaoergou batholith.

The chondrite-normalized Rare Earth Elements (REE) distribution patterns of the rhyolite and the Miaoergou batholith are generally identical (Fig. 8a). They are enriched in Light Rare Earth Elements (LREE) with significant negative Eu anomalies (partially insignificant) and an average δEu of only 0.20 ($\delta Eu=Eu_N/(Sm_N\times Gd_N)^{1/2}$). The total content of REE ranges from (144.14–187.85) ppm with an average of 170.83 ppm. The total LREE (ΣLREE, average of 136.32 ppm) is significantly higher than that of Heavy Rare Earth Elements (HREE, average of 34.51 ppm). The fractionation of LREE and HREE is significant, with a range of $(La/Yb)_N$ between 2.71–4.40 (average of 3.51). In the primitive mantle-normalized multi-element

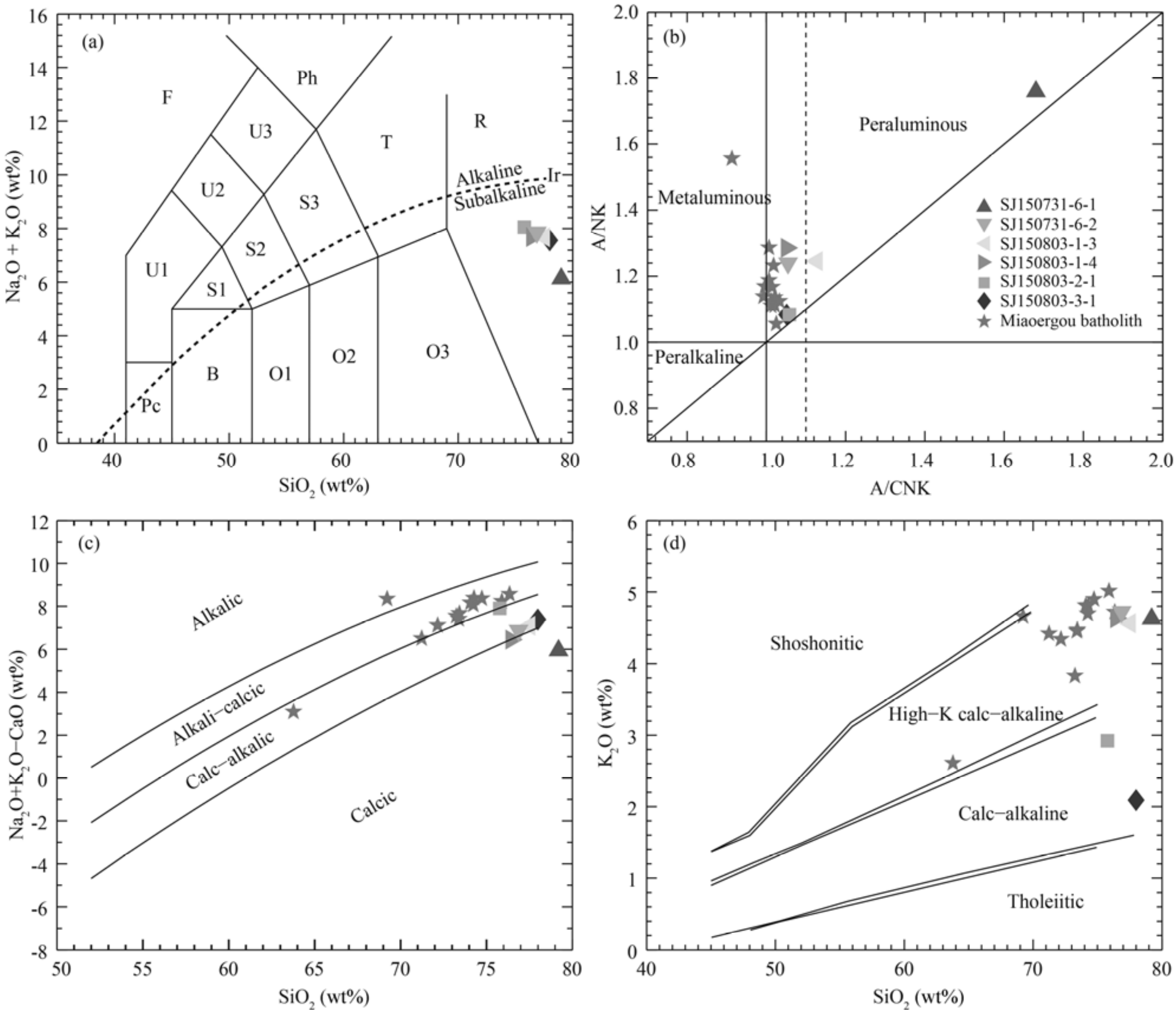

Fig. 6. (a) Igneous rock TAS (total alkali versus silica) classification diagram (after Middlemost, 1994); (b) A/CNK versus A/NK diagram (after Maniar and Piccoli 1989); (c) SiO_2 versus $Na_2O + K_2O - CaO$ diagram (after Frost et al., 2001); (d) SiO_2 versus K_2O diagram (after Rickwood, 1989).

Pc, Picrobasalt; B, Basalt; O1, Basaltic andesite; O2, Andesite; O3, Dacite; S1, Trachybasalt; S2, Basaltic trachyandesite; S3, Trachyandesite; T, Trachyte; F, Foidite; U1, Tephrite/Basanite; U2, Phonotephrite; U3, Tephriphonolite; R, Rhyolite; Ph, Phonolite; Ir, Irvine line. The date of Miaoergou batholith are from Huang et al. (2016).

spider diagram (Fig. 8b), rhyolite and Miaoergou batholith are both enriched in Large Ion Lithophile Elements (LILE), including enrichment in Rb, Ba, Th, U, and K, and are depleted in High Field Strength Elements (HFSE) such as Sr, Nb, Ta, Ti and P.

5 Zircon U-Pb Dating

5.1 Method

We separated zircons and then manually selected zircon grains with good crystal shapes as targets. Zircon cathodoluminescence (CL) images (Fig. 9) were taken with a JSM6510 scanning electron microscope. LA-MC-ICP-MS zircon U-Pb dating was completed at the Plasma Mass Spectrometry Laboratory of the Institute of Mineral Resources, Chinese Academy of Geological Sciences, Beijing, China, using a Finnigan Neptune-type MC-ICP-MS and the associated Newwave UP213 laser ablation system. We used the ICPMSDataCal program to process data (Table 3) and used the Isoplot 4.15 program for age calculation (Liu et al., 2008).

5.2 Results

The zircons from sample SJ150731-6-1 are 100–350 μm in length, prismatic, euhedral and show bright and dark stripes with developed rings and good crystallization (Fig. 9a), which is typical of the magmatic zircon. A total of 17 analyses were performed for this sample, and the resulting zircon U-Pb data are shown in Table 3. The contents of U and Th are (128.58–451.89) ppm and (75.69–183.14) ppm, respectively. The $^{232}Th/^{238}U$ ratio is 0.24–0.59, which is within the Th/U range of magmatic zircon

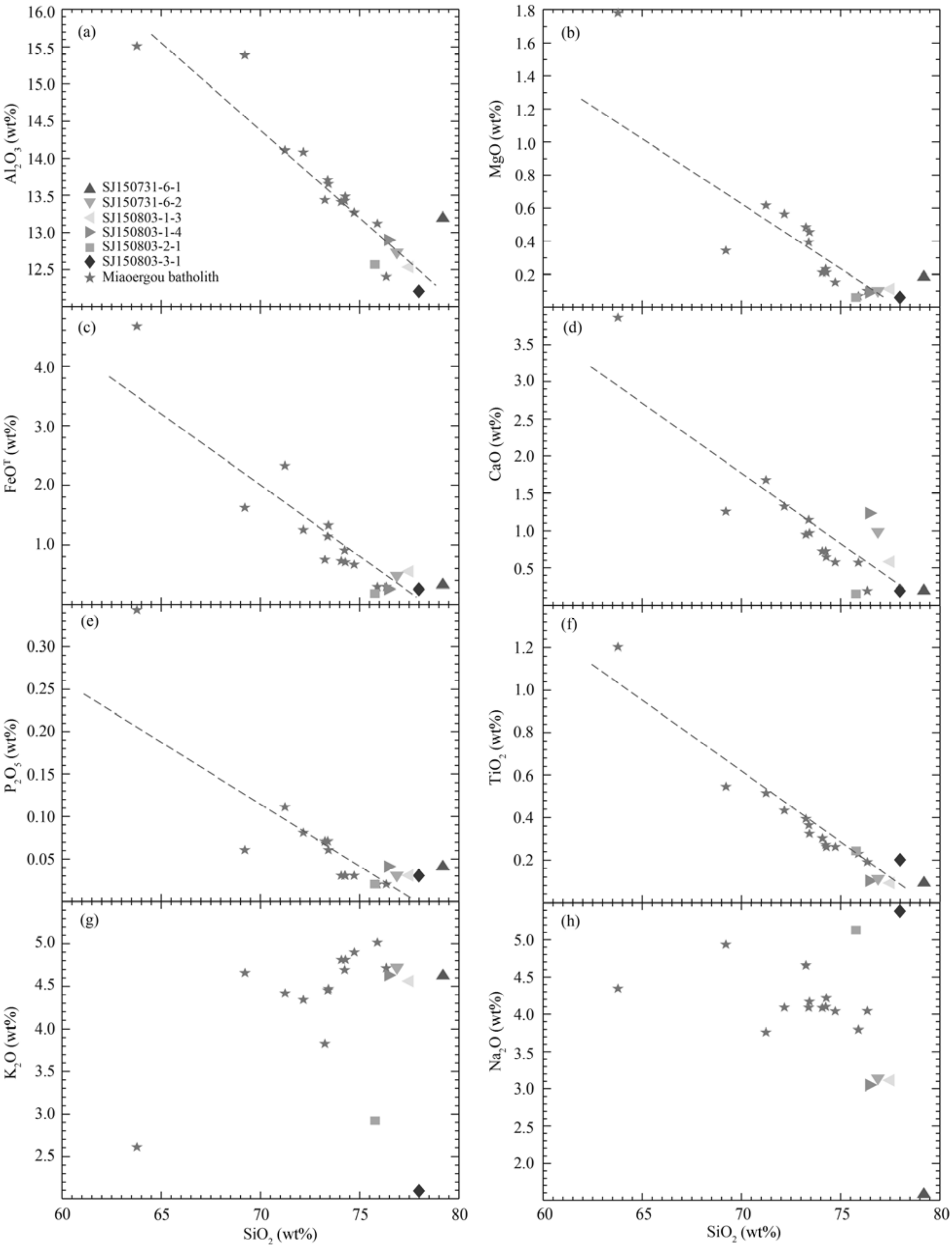

Fig. 7. Hark diagrams of the rhyolites.

(a) Al_2O_3 (wt%) versus SiO_2 (wt%); (b) MgO (wt%) versus SiO_2 (wt%); (c) FeO^T (wt%) versus SiO_2 (wt%); (d) CaO (wt%) versus SiO_2 (wt%); (e) Na_2O (wt%) versus SiO_2 (wt%); (f) TiO_2 (wt%) versus SiO_2 (wt%); (g), K_2O (wt%) versus SiO_2 (wt%); (h) P_2O_5 (wt%) versus SiO_2 (wt%). The date of Miaoergou batholith are from Huang et al. (2016).

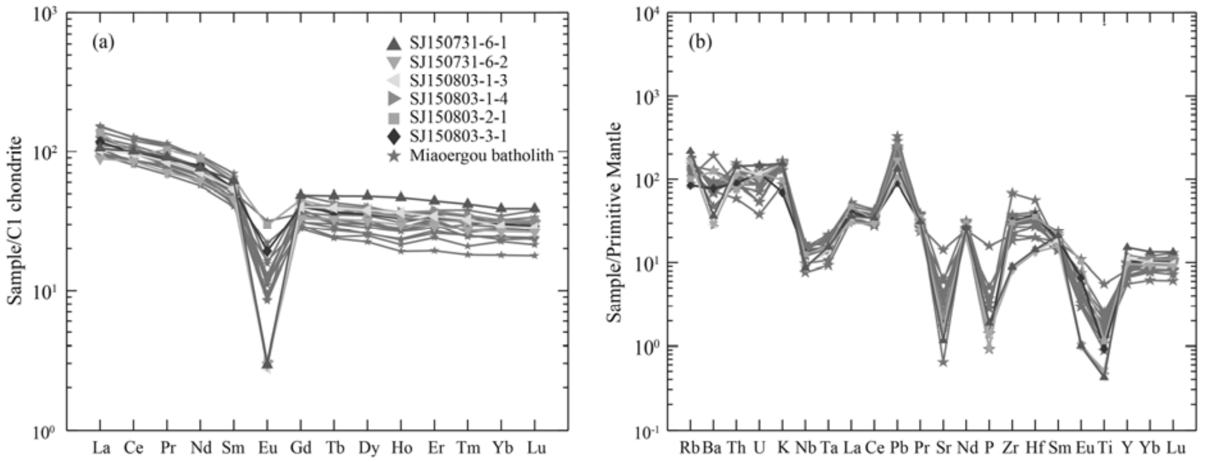

Fig. 8. Chondrite-normalized REE distribution patterns (a) and primitive mantle-normalized multi-element spider (b) diagram.
Chondrite and primitive mantle (the Silicate Earth–Pyrolite) values are taken from Sun and McDonough (1989). The date of Miaoergou batholith are from Huang et al. (2016).

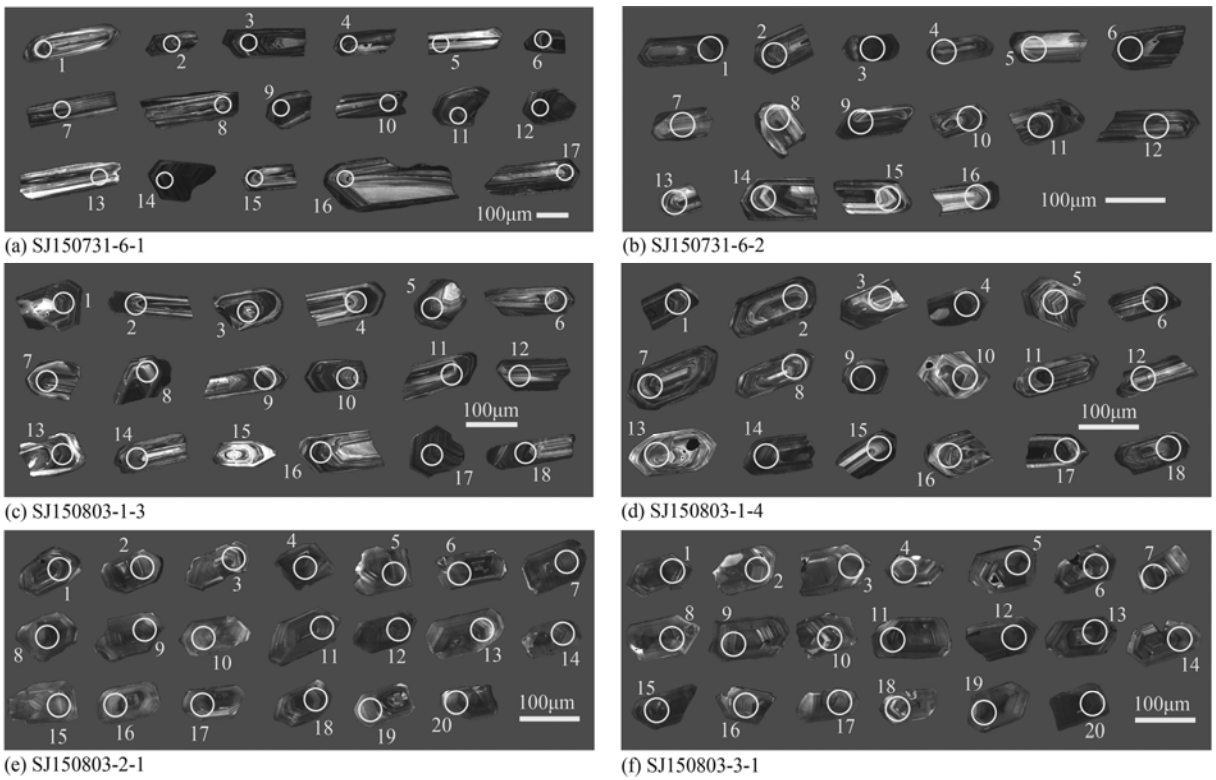

Fig. 9. Zircon CL images of rhyolite samples.
(a) sample SJ150731-6-1; (b) sample SJ150731-6-2; (c) sample SJ150803-1-3; (d) sample SJ150803-1-4; (e) sample SJ150803-2-1; (f) sample SJ150803-3-1.

(Hoskin and Black 2000; Belousova et al., 2002). The weighted average age of these 17 analyses is 295.9±1.9 Ma (MSWD=0.34, Fig. 10a).

The zircons from sample SJ150731-6-2 are 80–180 μm in length, prismatic, euhedral and show bright and dark stripes with developed rings and good crystallization (Fig. 9b), which is typical of the magmatic zircon. A total of 16 analyses were performed for this sample, and the resulting zircon U-Pb data are shown in Table 3. The contents of U and Th are (75.40–551.17) ppm and (29.97–200.08) ppm, respectively. The $^{232}Th/^{238}U$ ratio is 0.30–0.53, which is within the Th/U range of magmatic zircons (Hoskin and Black 2000; Belousova et al., 2002). The weighted average age of these 16 analyses is 310.97±1.9 Ma (MSWD=0.39, Fig. 10b).

The zircons from sample SJ150803-1-3 are 100–200 μm in length, prismatic, euhedral and show bright and dark stripes with developed rings and good crystallization (Fig. 9c), which is typical of the magmatic zircon. A total of 18 analyses were conducted for this sample, and the resulting zircon U-Pb data are shown in Table 3. The contents of U and Th are (94.06–749.15) ppm and (37.01–199.78) ppm, respectively. The $^{232}Th/^{238}U$ ratio is 0.26–0.59, which falls within the Th/U range of magmatic

Table 3 U-Pb isotope dating results for the zircons of rhyolite samples

Spot	Pb (ppm)	Th (ppm)	U (ppm)	$^{207}Pb/^{206}Pb$	1σ	$^{207}Pb/^{235}U$	1σ	$^{206}Pb/^{238}U$	1σ	Rho	Th/U	$^{207}Pb/^{206}Pb$ (Ma)	1σ	$^{206}Pb/^{238}U$ (Ma)	1σ	Concordance
SJ150731-6-1 (45°46′57.45″N, 83°38′41.34″E)																
1	13.54	95.58	277.00	0.05286	0.00077	0.34153	0.00582	0.04686	0.00052	0.6509	0.3451	324.13	26.85	295.24	3.20	98%
2	13.49	98.47	272.57	0.05311	0.00090	0.34499	0.00684	0.04719	0.00069	0.7338	0.3613	344.50	38.89	297.24	4.23	98%
3	22.16	148.31	439.45	0.05376	0.00073	0.35301	0.00651	0.04759	0.00060	0.6786	0.3375	361.17	29.63	299.73	3.67	97%
4	15.66	79.82	320.62	0.05325	0.00133	0.34323	0.00956	0.04691	0.00116	0.8868	0.2489	338.95	55.55	295.50	7.13	98%
5	15.35	124.77	298.74	0.05310	0.00106	0.34482	0.00935	0.04708	0.00087	0.6808	0.4177	331.54	44.44	296.56	5.35	98%
6	20.34	183.14	385.00	0.05334	0.00085	0.34583	0.00536	0.04712	0.00053	0.7265	0.4757	342.65	41.66	296.82	3.27	98%
7	12.58	123.07	235.74	0.05382	0.00119	0.34732	0.00791	0.04685	0.00058	0.5424	0.5220	364.87	45.37	295.14	3.56	97%
8	22.62	125.15	451.89	0.05204	0.00079	0.33730	0.00673	0.04699	0.00064	0.6830	0.2769	287.10	33.33	296.00	3.94	99%
9	15.01	117.17	287.39	0.05307	0.00108	0.34755	0.00859	0.04744	0.00058	0.4986	0.4077	331.54	46.29	298.78	3.60	98%
10	16.95	112.00	334.55	0.05199	0.00084	0.33224	0.00576	0.04645	0.00057	0.7066	0.3348	283.40	32.41	292.67	3.51	99%
11	18.55	130.47	359.20	0.05339	0.00084	0.34527	0.00730	0.04692	0.00072	0.7265	0.3632	346.35	39.81	295.60	4.44	98%
12	7.13	75.69	128.58	0.05258	0.00186	0.34333	0.01252	0.04746	0.00075	0.4342	0.5887	309.32	81.47	298.92	4.62	99%
13	13.63	137.94	254.13	0.05208	0.00137	0.33487	0.00882	0.04680	0.00074	0.6035	0.5428	300.06	59.25	294.81	4.58	99%
14	10.96	76.98	210.80	0.05218	0.00089	0.33408	0.00591	0.04656	0.00050	0.6044	0.3652	294.51	38.89	293.35	3.07	99%
15	13.16	99.26	252.81	0.05434	0.00152	0.34632	0.00933	0.04634	0.00066	0.5255	0.3926	387.09	67.59	291.98	4.04	96%
16	13.10	97.79	249.01	0.05411	0.00176	0.34697	0.00898	0.04682	0.00087	0.7192	0.3927	375.98	76.85	294.99	5.37	97%
17	11.98	79.84	227.96	0.05180	0.00151	0.33863	0.01058	0.04746	0.00082	0.5499	0.3502	275.99	66.66	298.94	5.02	99%
SJ150731-6-2 (45°46′57.45″N, 83°38′41.34″E)																
1	21.61	137.36	391.66	0.05315	0.00155	0.36582	0.00984	0.04996	0.00068	0.5075	0.3507	344.50	66.66	314.27	4.19	99%
2	15.00	95.62	272.10	0.05299	0.00197	0.36505	0.01283	0.05001	0.00067	0.3784	0.3514	327.84	83.33	314.58	4.08	99%
3	22.72	200.08	396.11	0.05263	0.00099	0.36316	0.00863	0.05012	0.00126	0.6000	0.5051	322.28	10.19	315.24	7.71	99%
4	13.45	92.97	242.28	0.05342	0.00124	0.36417	0.00797	0.04970	0.00080	0.7391	0.3837	346.35	51.85	312.68	4.94	99%
5	4.19	29.97	75.40	0.05248	0.00204	0.35978	0.01551	0.04961	0.00068	0.3192	0.3975	305.62	87.03	312.14	4.19	99%
6	20.39	152.06	363.41	0.05332	0.00080	0.36567	0.00666	0.04978	0.00067	0.7399	0.4184	342.65	33.33	313.15	4.12	98%
7	5.76	42.34	103.28	0.05278	0.00161	0.36123	0.01312	0.04954	0.00079	0.4367	0.4099	320.43	65.74	311.69	4.83	99%
8	11.44	73.32	210.66	0.05305	0.00096	0.36305	0.00770	0.04967	0.00063	0.6008	0.3481	331.54	36.11	312.47	3.89	99%
9	14.79	83.10	275.27	0.05389	0.00101	0.36664	0.00748	0.04945	0.00057	0.5690	0.3019	364.87	42.59	311.16	3.52	98%
10	19.90	148.13	360.50	0.05365	0.00178	0.36230	0.01371	0.04889	0.00062	0.3347	0.4109	366.72	74.07	307.72	3.81	98%
11	4.42	36.47	78.39	0.05411	0.00189	0.36486	0.01283	0.04895	0.00058	0.3351	0.4653	375.98	79.62	308.10	3.54	97%
12	13.03	93.18	236.51	0.05390	0.00149	0.36327	0.01166	0.04877	0.00055	0.3487	0.3940	368.57	62.96	306.99	3.35	97%
13	29.67	175.93	551.17	0.05267	0.00102	0.35471	0.00566	0.04899	0.00064	0.8220	0.3192	322.28	16.67	308.30	3.95	99%
14	9.84	65.27	179.55	0.05405	0.00120	0.36633	0.00888	0.04916	0.00053	0.4487	0.3635	372.28	56.48	309.35	3.29	97%
15	8.78	49.14	162.63	0.05381	0.00106	0.36596	0.00786	0.04933	0.00053	0.5007	0.3022	364.87	44.44	310.39	3.26	98%
16	12.60	116.69	220.48	0.05329	0.00126	0.36346	0.00910	0.04947	0.00062	0.4985	0.5293	342.65	53.70	311.24	3.79	98%
SJ150803-1-3 (45°46′57.67″N, 83°38′44.12″E)																
1	22.53	174.76	423.95	0.05427	0.00094	0.35114	0.00764	0.04692	0.00072	0.7020	0.4122	383.39	38.89	295.60	4.42	96%
2	33.07	194.08	641.15	0.05337	0.00077	0.34972	0.00803	0.04747	0.00081	0.7398	0.3027	342.65	26.85	298.95	4.96	98%
3	17.85	121.17	349.07	0.05339	0.00121	0.34445	0.00913	0.04676	0.00073	0.5854	0.3471	346.35	50.00	294.57	4.47	97%
4	38.78	199.78	749.15	0.05435	0.00123	0.36034	0.00823	0.04808	0.00062	0.5628	0.2667	387.09	45.37	302.71	3.80	96%
5	4.92	37.57	94.06	0.05313	0.00129	0.34553	0.00967	0.04717	0.00071	0.5377	0.3994	344.50	53.70	297.13	4.37	98%
6	16.54	132.83	317.07	0.05392	0.00083	0.35160	0.00673	0.04724	0.00051	0.5674	0.4189	368.57	67.59	297.55	3.16	97%
7	26.70	166.01	521.95	0.05235	0.00059	0.34620	0.00525	0.04803	0.00063	0.8648	0.3181	301.91	25.92	302.41	3.88	99%
8	12.52	103.21	239.41	0.05184	0.00085	0.33848	0.00681	0.04731	0.00057	0.5940	0.4311	279.69	41.66	297.98	3.48	99%
9	18.97	125.49	371.15	0.05342	0.00069	0.34954	0.00552	0.04746	0.00054	0.7212	0.3381	346.35	29.63	298.89	3.33	98%
10	15.07	79.79	286.36	0.05211	0.00099	0.33722	0.00831	0.04684	0.00058	0.4992	0.2786	300.06	37.96	295.11	3.55	99%
11	14.59	149.99	257.36	0.05393	0.00204	0.34853	0.01026	0.04702	0.00082	0.5953	0.5828	368.57	85.18	296.19	5.07	97%
12	11.62	87.74	211.44	0.05200	0.00150	0.33872	0.00957	0.04724	0.00053	0.3989	0.4150	287.10	66.66	297.58	3.28	99%
13	18.05	151.95	324.67	0.05441	0.00086	0.35147	0.00549	0.04687	0.00046	0.6257	0.4680	387.09	39.81	295.26	2.82	96%
14	5.46	37.01	102.07	0.05375	0.00140	0.34954	0.01010	0.04714	0.00061	0.4463	0.3626	361.17	57.40	296.91	3.74	97%
15	22.28	124.55	420.55	0.05251	0.00081	0.34175	0.00542	0.04721	0.00041	0.5443	0.2962	309.32	35.18	297.40	2.51	99%
16	13.25	70.67	249.84	0.05271	0.00078	0.34580	0.00540	0.04762	0.00048	0.6506	0.2829	316.73	33.33	299.91	2.98	99%
17	15.78	122.95	290.98	0.05366	0.00113	0.34770	0.00722	0.04701	0.00066	0.6801	0.4225	366.72	78.70	296.17	4.09	97%
18	5.23	39.95	96.04	0.05316	0.00132	0.34661	0.00882	0.04739	0.00058	0.4793	0.4159	344.50	55.55	298.48	3.56	98%
SJ150803-1-4 (45°46′57.67″N, 83°38′44.12″E)																
1	5.95	52.56	115.04	0.05392	0.00122	0.34724	0.01021	0.04668	0.00087	0.6354	0.4569	368.57	50.00	294.13	5.37	97%
2	4.03	38.83	76.05	0.05408	0.00230	0.35474	0.01654	0.04749	0.00073	0.3309	0.5106	375.98	100.92	299.06	4.51	96%
3	13.29	89.55	264.85	0.05234	0.00115	0.33483	0.00654	0.04654	0.00060	0.6585	0.3381	301.91	50.00	293.24	3.69	99%
4	14.10	85.56	280.22	0.05408	0.00085	0.34907	0.00688	0.04676	0.00053	0.5801	0.3053	375.98	35.18	294.59	3.29	96%
5	24.62	179.86	479.58	0.05394	0.00067	0.34839	0.00458	0.04693	0.00057	0.9241	0.3750	368.57	27.78	295.66	3.51	97%
6	16.90	110.90	330.03	0.05367	0.00094	0.34884	0.01041	0.04708	0.00087	0.6207	0.3360	366.72	38.89	296.59	5.37	97%
7	13.26	84.64	260.21	0.05262	0.00082	0.33759	0.00664	0.04649	0.00062	0.6730	0.3253	322.28	35.18	292.96	3.79	99%
8	19.50	228.77	354.30	0.05267	0.00074	0.34001	0.00609	0.04676	0.00054	0.6494	0.6457	322.28	31.48	294.62	3.35	99%
9	13.40	81.61	261.04	0.05272	0.00085	0.34175	0.00766	0.04705	0.00086	0.8200	0.3126	316.73	37.04	296.41	5.32	99%
10	23.91	186.43	463.11	0.05441	0.00131	0.34483	0.01214	0.04604	0.00144	0.8897	0.4026	387.09	55.55	290.19	8.89	96%
11	2.84	19.76	54.04	0.05388	0.00169	0.34698	0.01163	0.04682	0.00080	0.5105	0.3656	364.87	70.36	294.96	4.93	97%
12	18.92	139.93	358.29	0.05380	0.00087	0.34335	0.00613	0.04661	0.00094	0.6000	0.3905	361.17	37.04	293.67	5.78	97%
13	18.19	121.43	349.05	0.05323	0.00090	0.34402	0.00693	0.04699	0.00085	0.8974	0.3479	338.95	38.89	296.03	5.23	98%
14	19.50	110.08	376.93	0.05323	0.00082	0.34336	0.00694	0.04686	0.00077	0.8134	0.2921	338.95	35.18	295.19	4.74	98%
15	6.15	39.76	118.89	0.05452	0.00134	0.34867	0.00854	0.04649	0.00058	0.5068	0.3344	390.79	55.55	292.96	3.55	96%
16	15.92	94.68	311.43	0.05324	0.00078	0.34323	0.00633	0.04676	0.00060	0.6939	0.3040	338.95	33.33	294.60	3.69	98%

Continued Table 3

Spot	Pb (ppm)	Th (ppm)	U (ppm)	$^{207}Pb/^{206}Pb$	1σ	$^{207}Pb/^{235}U$	1σ	$^{206}Pb/^{238}U$	1σ	Rho	Th/U	$^{207}Pb/^{206}Pb$ (Ma)	1σ	$^{206}Pb/^{238}U$ (Ma)	1σ	Concordance
17	13.59	87.35	261.69	0.05408	0.00088	0.34832	0.00627	0.04668	0.00045	0.5351	0.3338	375.98	32.41	294.11	2.77	96%
18	18.63	158.69	348.36	0.05373	0.00126	0.34489	0.00674	0.04657	0.00062	0.6852	0.4555	361.17	53.70	293.44	3.84	97%
SJ150803-2-1 (45°47′13.47″N, 83°38′36.51″E)																
1	10.97	97.00	198.16	0.05262	0.00112	0.35537	0.00926	0.04892	0.00083	0.6546	0.4895	322.28	48.14	307.92	5.13	99%
2	10.40	95.26	187.30	0.05210	0.00092	0.35221	0.00811	0.04898	0.00077	0.6852	0.5086	300.06	37.96	308.23	4.75	99%
3	8.26	77.70	150.19	0.05479	0.00211	0.36321	0.01314	0.04826	0.00091	0.5195	0.5173	466.71	82.40	303.81	5.58	96%
4	7.98	67.39	149.02	0.05433	0.00179	0.35992	0.01254	0.04801	0.00069	0.4120	0.4522	383.39	74.07	302.29	4.24	96%
5	11.52	149.30	196.89	0.05145	0.00120	0.34961	0.00867	0.04929	0.00064	0.5212	0.7583	261.18	58.33	310.14	3.91	98%
6	12.14	151.41	210.82	0.05309	0.00104	0.35408	0.00853	0.04837	0.00084	0.7224	0.7182	331.54	44.44	304.51	5.18	98%
7	11.93	129.54	214.01	0.05251	0.00152	0.35381	0.01036	0.04887	0.00061	0.4268	0.6053	309.32	66.66	307.58	3.75	99%
8	10.88	124.16	195.21	0.05480	0.00107	0.36293	0.00804	0.04802	0.00060	0.5619	0.6360	466.71	44.44	302.37	3.68	96%
9	17.27	257.75	289.12	0.05249	0.00078	0.35089	0.00688	0.04841	0.00060	0.6307	0.8915	305.62	33.33	304.76	3.68	99%
10	6.62	53.52	126.56	0.05444	0.00120	0.36118	0.00872	0.04819	0.00067	0.5727	0.4229	390.79	50.00	303.42	4.10	96%
11	13.35	131.50	249.77	0.05370	0.00083	0.35553	0.00563	0.04811	0.00052	0.6815	0.5265	366.72	35.18	302.90	3.20	98%
12	8.50	78.27	161.35	0.05376	0.00103	0.35347	0.00654	0.04780	0.00053	0.6034	0.4851	361.17	74.99	301.02	3.28	97%
13	18.52	213.23	338.26	0.05317	0.00080	0.35445	0.00647	0.04833	0.00051	0.5808	0.6304	344.50	33.33	304.26	3.15	98%
14	7.49	60.89	143.30	0.05242	0.00141	0.34565	0.00909	0.04791	0.00052	0.4153	0.4249	301.91	61.11	301.69	3.22	99%
15	8.19	73.14	154.05	0.05438	0.00129	0.35509	0.00890	0.04743	0.00057	0.4790	0.4748	387.09	53.70	298.73	3.50	96%
16	11.76	133.90	210.27	0.05437	0.00117	0.35944	0.00792	0.04798	0.00053	0.4995	0.6368	387.09	45.37	302.08	3.25	96%
17	7.80	72.06	145.53	0.05233	0.00118	0.34561	0.00908	0.04794	0.00065	0.5145	0.4952	298.21	47.22	301.84	3.98	99%
18	9.92	86.39	181.84	0.05352	0.00098	0.35750	0.00640	0.04856	0.00061	0.6986	0.4751	350.06	40.74	305.66	3.73	98%
19	8.13	64.33	151.17	0.05329	0.00088	0.35481	0.00678	0.04828	0.00051	0.5572	0.4256	342.65	43.52	303.94	3.16	98%
20	13.37	149.36	234.70	0.05517	0.00179	0.36395	0.01674	0.04769	0.00084	0.3846	0.6364	420.42	76.85	300.31	5.19	95%
SJ150803-3-1 (45°47′12.25″N, 83°38′39.01″E)																
1	12.07	126.92	211.65	0.05462	0.00099	0.36049	0.00737	0.04785	0.00055	0.5670	0.5997	398.20	40.74	301.31	3.41	96%
2	10.49	110.20	183.05	0.05413	0.00110	0.36116	0.00943	0.04820	0.00059	0.4716	0.6020	375.98	44.44	303.46	3.65	96%
3	10.29	112.12	180.48	0.05309	0.00100	0.35167	0.00737	0.04801	0.00055	0.5451	0.6212	331.54	37.96	302.30	3.37	98%
4	10.61	105.42	191.75	0.05257	0.00136	0.34637	0.00923	0.04776	0.00047	0.3701	0.5498	309.32	59.25	300.78	2.90	99%
5	7.36	65.89	135.60	0.05458	0.00143	0.35769	0.00891	0.04760	0.00055	0.4679	0.4860	394.50	54.63	299.78	3.41	96%
6	17.88	254.56	303.74	0.05337	0.00076	0.34783	0.00651	0.04743	0.00089	0.6000	0.8381	346.35	26.85	298.75	5.50	98%
7	9.27	86.93	165.85	0.05276	0.00269	0.35375	0.01365	0.04904	0.00115	0.6085	0.5242	316.73	116.65	308.65	7.07	99%
8	8.91	84.80	162.96	0.05465	0.00166	0.35738	0.01180	0.04741	0.00075	0.4759	0.5203	398.20	68.51	298.60	4.59	96%
9	8.28	60.97	155.06	0.05371	0.00159	0.35924	0.01285	0.04855	0.00109	0.6301	0.3932	366.72	66.66	305.63	6.72	98%
10	8.19	60.62	155.92	0.05287	0.00219	0.34739	0.01499	0.04768	0.00116	0.5648	0.3888	324.13	89.81	300.25	7.15	99%
11	12.37	114.46	228.00	0.05257	0.00091	0.34928	0.00632	0.04834	0.00071	0.8062	0.5020	309.32	8.33	304.31	4.34	99%
12	8.06	67.03	152.09	0.05508	0.00187	0.36318	0.01325	0.04775	0.00072	0.4123	0.4407	416.72	80.55	300.68	4.42	95%
13	15.46	197.66	272.98	0.05176	0.00127	0.33921	0.00870	0.04755	0.00069	0.5676	0.7241	275.99	57.40	299.43	4.26	99%
14	16.93	202.36	301.59	0.05310	0.00087	0.35132	0.00765	0.04796	0.00084	0.8060	0.6710	331.54	37.03	301.96	5.18	98%
15	11.87	135.47	212.64	0.05375	0.00104	0.35500	0.00775	0.04793	0.00071	0.6788	0.6371	361.17	74.99	301.79	4.37	97%
16	11.60	98.70	215.10	0.05582	0.00216	0.36367	0.01418	0.04730	0.00100	0.5399	0.4589	455.60	80.55	297.91	6.13	94%
17	9.30	92.11	169.80	0.05485	0.00148	0.36168	0.00822	0.04813	0.00073	0.6645	0.5425	405.61	59.26	303.00	4.47	96%
18	9.41	96.58	172.05	0.05306	0.00153	0.35212	0.01060	0.04810	0.00057	0.3941	0.5613	331.54	64.81	302.87	3.51	98%
19	20.62	231.99	374.29	0.05341	0.00088	0.35301	0.00649	0.04792	0.00056	0.6309	0.6198	346.35	37.03	301.74	3.42	98%
20	14.92	198.52	265.03	0.05598	0.00149	0.36642	0.01097	0.04744	0.00093	0.6534	0.7490	450.05	59.26	298.78	5.71	94%

zircon (Hoskin and Black 2000; Belousova et al., 2002). The weighted average age of the 18 analyses is 297.7±1.6 Ma (MSWD=0.37, Fig. 10c).

The zircons from sample SJ150803-1-4 are 80–180 μm in length, prismatic, euhedral and show bright and dark stripes with developed rings and good crystallization (Fig. 9d), which is typical of the magmatic zircon. A total of 18 analyses were conducted for this sample, and the resulting zircon U-Pb data are shown in Table 3. The contents of U and Th are (54.04–479.58) ppm and (19.76–228.77) ppm, respectively. The $^{232}Th/^{238}U$ ratio is 0.29–0.65, which falls within the Th/U range of magmatic zircon (Hoskin and Black 2000; Belousova et al., 2002). The weighted average age of the 18 analyses is 294.5±1.9 Ma (MSWD=0.14, Fig. 10d).

The zircons from sample SJ150803-2-1 are 100–120 μm in length, prismatic, euhedral and show bright and dark stripes with developed rings and good crystallization (Fig. 9e), which is typical of the magmatic zircon. A total of 20 analyses were conducted for this sample, and the resulting zircon U-Pb data are shown in Table 3. The contents of U and Th is (126.56–338.26) ppm and (53.52–257.75) ppm, respectively. The $^{232}Th/^{238}U$ ratio is 0.42–0.90, which falls within the Th/U range of magmatic zircon (Hoskin and Black 2000; Belousova et al., 2002). The weighted average age of the 20 analyses is 303.6±1.7 Ma (MSWD=0.53, Fig. 10e).

The zircons from sample SJ150803-3-1 are 100–120 μm in length, prismatic, euhedral and show bright and dark stripes with developed rings and good crystallization (Fig. 9f), which is typical of the magmatic zircon. A total of 20 analyses were conducted for this sample, and the resulting zircon U-Pb data are shown in Table 3. The contents of U and Th are (135.60–374.29) ppm and (60.62–254.56) ppm, respectively. The $^{232}Th/^{238}U$ ratio is 0.38–0.84, which falls within the Th/U range of magmatic zircon (Hoskin and Black 2000; Belousova et al., 2002). The weighted average age of the 20 analyses is 301.5±1.9 Ma (MSWD=0.23, Fig. 10f).

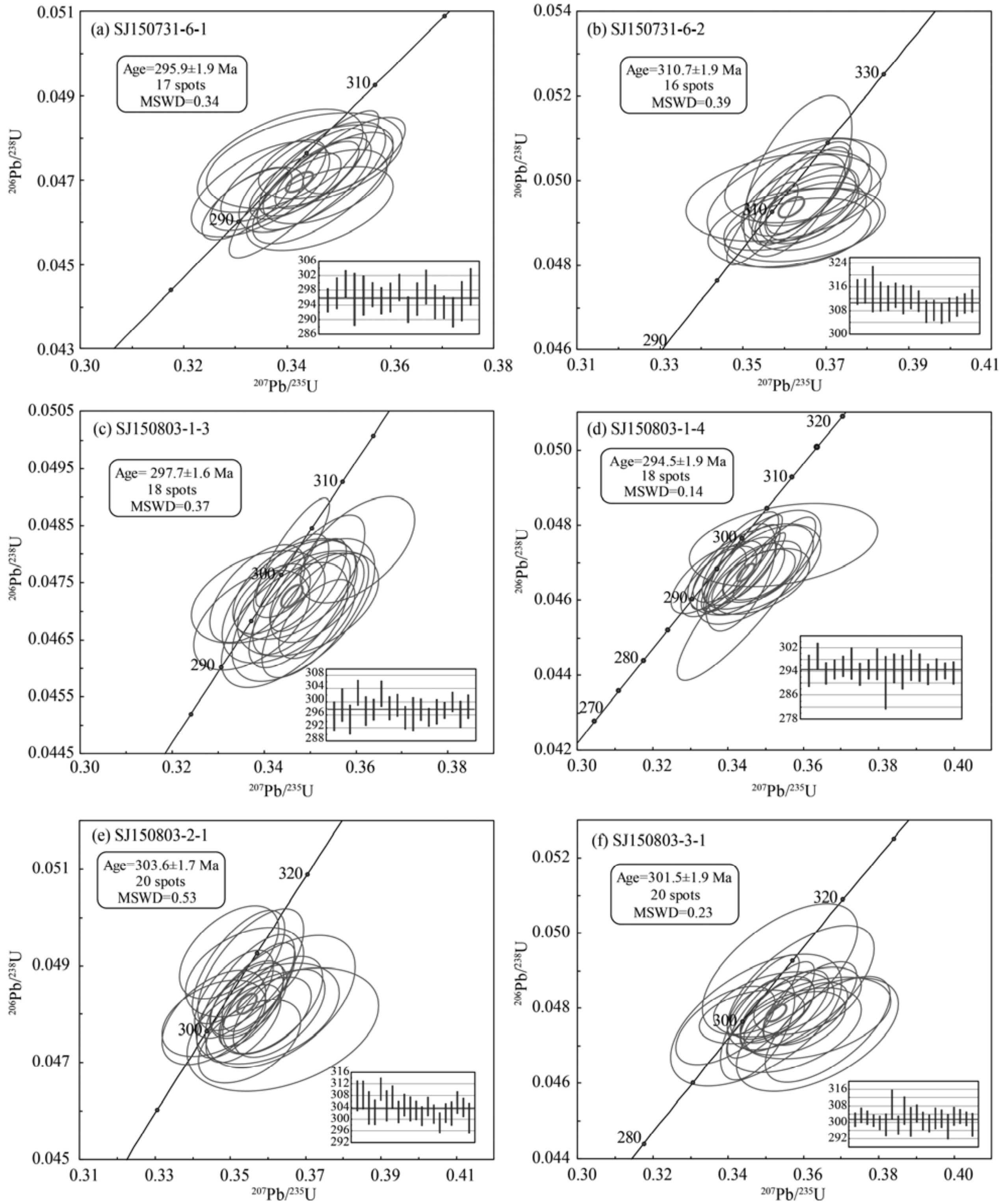

Fig. 10. Zircon U-Pb isotopic data of rhyolite samples.
(a) sample SJ150731-6-1; (b) sample SJ150731-6-2; (c) sample SJ150803-1-3; (d) sample SJ150803-1-4; (e) sample SJ150803-2-1; (f) sample SJ150803-3-1.

6 Discussion

6.1 Tectonic environment identification

In the A-type granite identification diagram, the rhyolite and Miaoergou batholith both are A-type granites (Fig. 11). In the A1 and A2 types granite identification diagram, the rhyolite shows A2-type characteristics (Fig. 12). According to the different geochemical characteristics, A-type granites can be divided into A1 and A2 types (Eby, 1992), which are formed in different tectonic environments. A1-type magma is formed by differentiation during the intrusion of mantle magma into continent rifts or plates, which shares the same origin as oceanic island magma. A2-type granite magma is generally derived from the continental crust, which is related to continent-continent collision or island arc magmatism (Su et al., 2006; Huang et al., 2016). The rhyolite may have been derived from magma formed

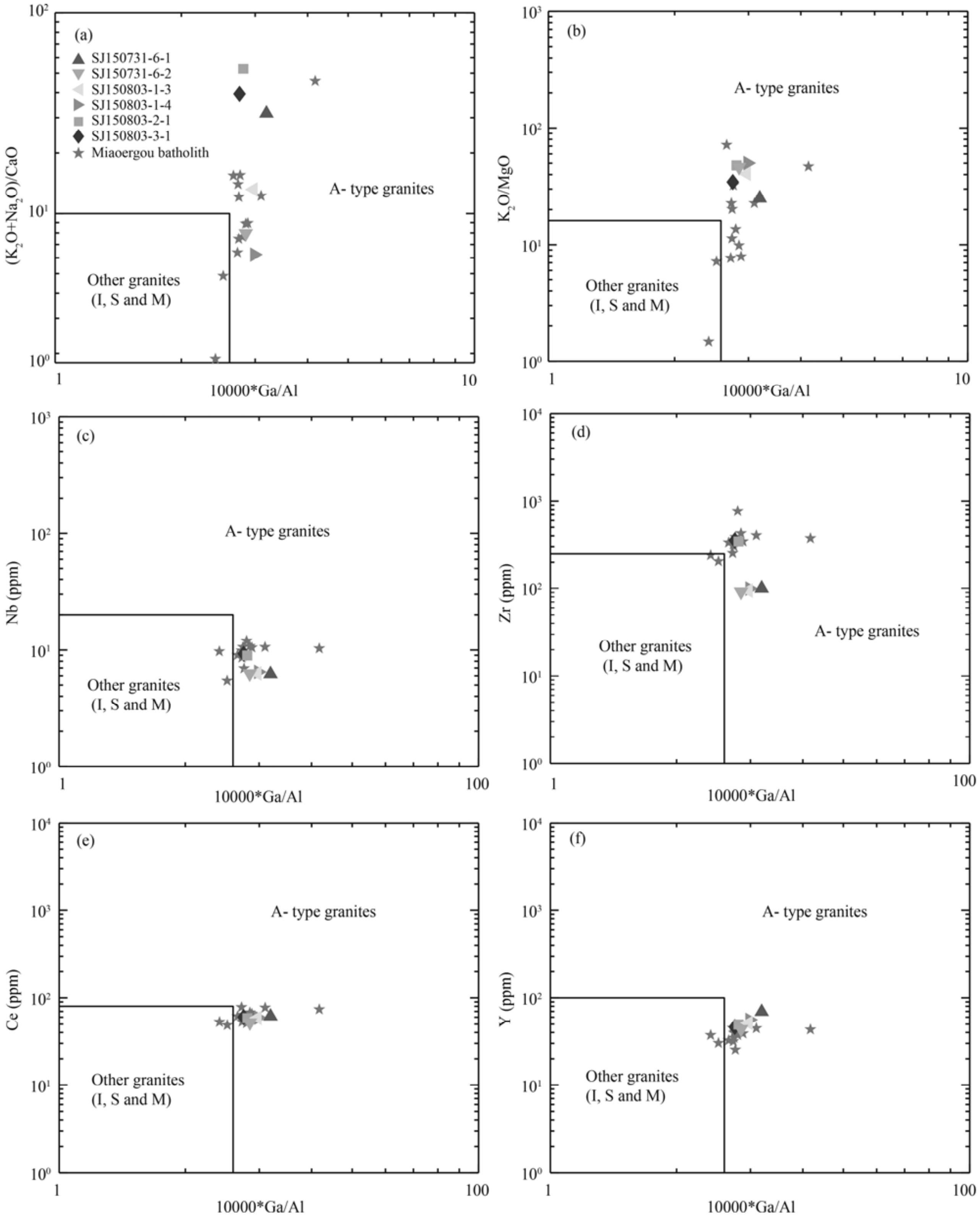

Fig. 11. A-type classification diagrams of the rhyolites from the West Junggar area (after Whalen et al., 1987).

(a) (K_2O + Na_2O)/CaO versus 10000*Ga/Al diagram; (b) K_2O/MgO versus 10000*Ga/Al diagram; (c) Nb versus 10000*Ga/Al diagram; (d) Zr versus 10000*Ga/Al diagram; (e) Ce versus 10000*Ga/Al diagram; (f) Y versus 10000*Ga/Al diagram. The date of Miaoergou batholith are from Huang et al. (2016).

beneath the Kazakhstan micro-plate, characterized by a significant amount mixing of continental crust materials. The trace element tectonic environment identification diagram (Pearce et al., 1984) indicates that, similar to the Miaoergou batholith, the rhyolite was formed in a post-orogenic extensional tectonic environment (Fig. 13).

Previous researchers concluded that the tectonic environment of the West Junggar area mainly consists of oceanic ridge environment, island arc environment and post-orogenic extensional tectonic environment during the Late Paleozoic. Some researchers insisted that the oceanic ridge environment still existed in the Late Paleozoic (Tang et al., 2009, 2010a, b; Geng et al., 2011). Among them, Geng et al. (2011) suggested that oceanic ridge subduction was subsequent to volcanic eruptions in the Early Carboniferous (331–344 Ma). Some researchers believed that the island arcs were also widely distributed in the Late Carboniferous–Early Permian, proved by the adakite–high -Mg andesite–Nb-enriched basaltic suites and large amounts of calc-alkaline magmatism associated with subduction (Xiao et al., 2006, 2008; Liu et al., 2009). Besides, some researchers summarized that the post-collisional orogeny of the West Junggar area started from the Late Carboniferous and lasted until the Early Permian (Han et al., 2006; Zhou et al.,2008; Chen et al.,2010; Huang et al., 2016). The granite magmatism was strongest during the Late Carboniferous–Early Permian and rarely occurred in the late Late Permian in the West Junggar area. Furthermore, there was no metamorphism associated with subduction in this area. Therefore, based on the previous findings and the geochemical characteristics of rhyolite, we conclude that the West Junggar area was under the post-orogenic extensional tectonic environment during the Late Carboniferous–Early Permian.

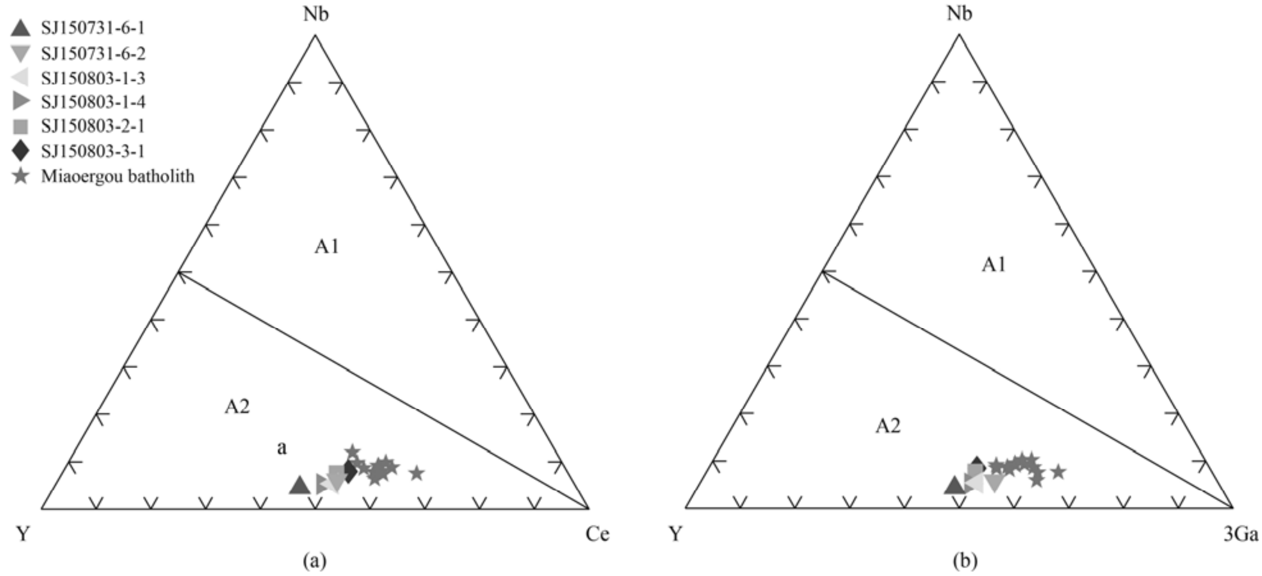

Fig. 12. A1-type and A2-type classification diagrams of the rhyolites from the West Junggar area (after Eby 1992). (a) Diagram Nb–Y–Ce; (b) Diagram Nb–Y–3Ga. The date of Miaoergou batholith are from Huang et al. (2016).

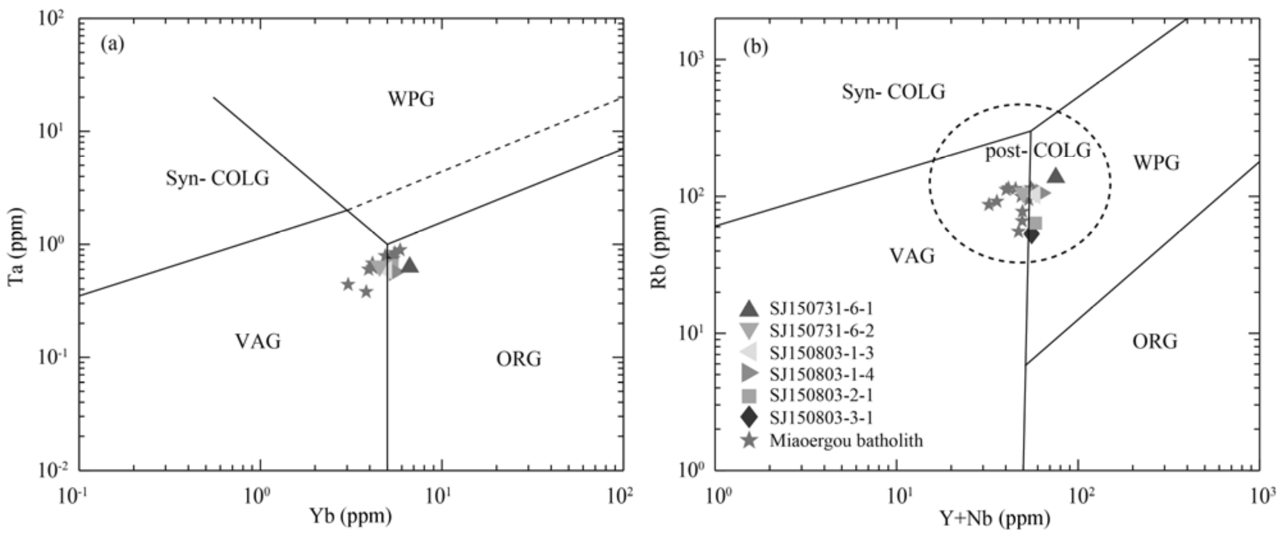

Fig. 13. Trace element discrimination diagrams for the tectonic interpretation of the West Junggar area.
(a) Ta versus Yb; (b) Rb versus (Y + Nb) (after Pearce et al., 1984; Pearce, 1996). Syn-COLG, syn-collisional granites; VAG, volcanic arc granites; WPG, within-plate granites; ORG, ocean ridge granites; post-COLG, post collisional granites. The date of Miaoergou batholith are from Huang et al. (2016).

6.2 Stratigraphic sequence analysis

Zircon U-Pb dating results show that the rhyolites on the northwestern side of the Miaoergou batholith, from the rhyolite with rhyolitic structure and columnar joint at the bottom to the thick, laminar, record acidic volcanic-magmatic activity during the Late Carboniferous–Early Permian, between 303.6 Ma and 294.5 Ma. The zircon U-Pb age (310.7 Ma) of sample SJ150731-6-2, which is located in the middle of the sequence, is far older than the age of sample SJ150731-6-1 (295.9 Ma) from the same sampling location. This may reflect the age of inherited zircons from earlier magmatic activities in Miaoergou batholith, which have the same origin as the rhyolite. Therefore, except for sample SJ150731-6-2, all other rhyolite samples generally show normal sequence characteristics.

6.3 Discussion on the columnar joint of rhyolite

The occurrence of rhyolite is mainly confined to continental margins, marginal seas and island arcs. Calc-alkaline series rhyolites mainly occur in island arcs, active continental margins and intracontinental orogenic belts and usually coexist with tuff, andesitic tuff, and andesite (Zhang et al., 2012). For example, the Cenozoic rhyolite that developed in the Aso volcano, Japan is mainly subject to the effects of subduction of the West Pacific plate (Kouzi and Kazunori, 1983; Nakada and Kamata, 1991; Miyoshi et al., 2011). A large number of Jurassic and Cretaceous rhyolites are distributed in the coastal part of eastern China, forming an expansive paleo-volcanic belt that is oriented north–south (Hu, 1992; Xing et al., 1999). This belt may be closely linked to subduction of the West Pacific plate beneath the Eurasian continent.

Previous researches regarding rhyolite structure mainly focused on the rhyolitic structure and lithophysa structure, whereas studies of the columnar joints were few. In addition, studies regarding magmatic columnar joints have mainly focused on columnar jointed basalt, and less attention has been paid to columnar jointed rhyolite. In addition, previous scholars have considered the development of columnar joints as a phenomenon unique to basalt, which has a low viscosity and strong flow. Research has shown that, similar to basalt, rhyolite with high viscosity and weak flow could also develop columnar joints (Xu, 1995). For example, a large number of columnar jointed rhyolites occur in the West Pacific ocean -continent transition zone, which are mainly Jurassic–Cretaceous. Areas including Zhejiang Jinyunxiandu and Linhai (Xu, 1995), Jilin Siping (Zhang, 2001; Li et al., 2007) and Hong Kong (Fang et al., 2011; Xing et al.,

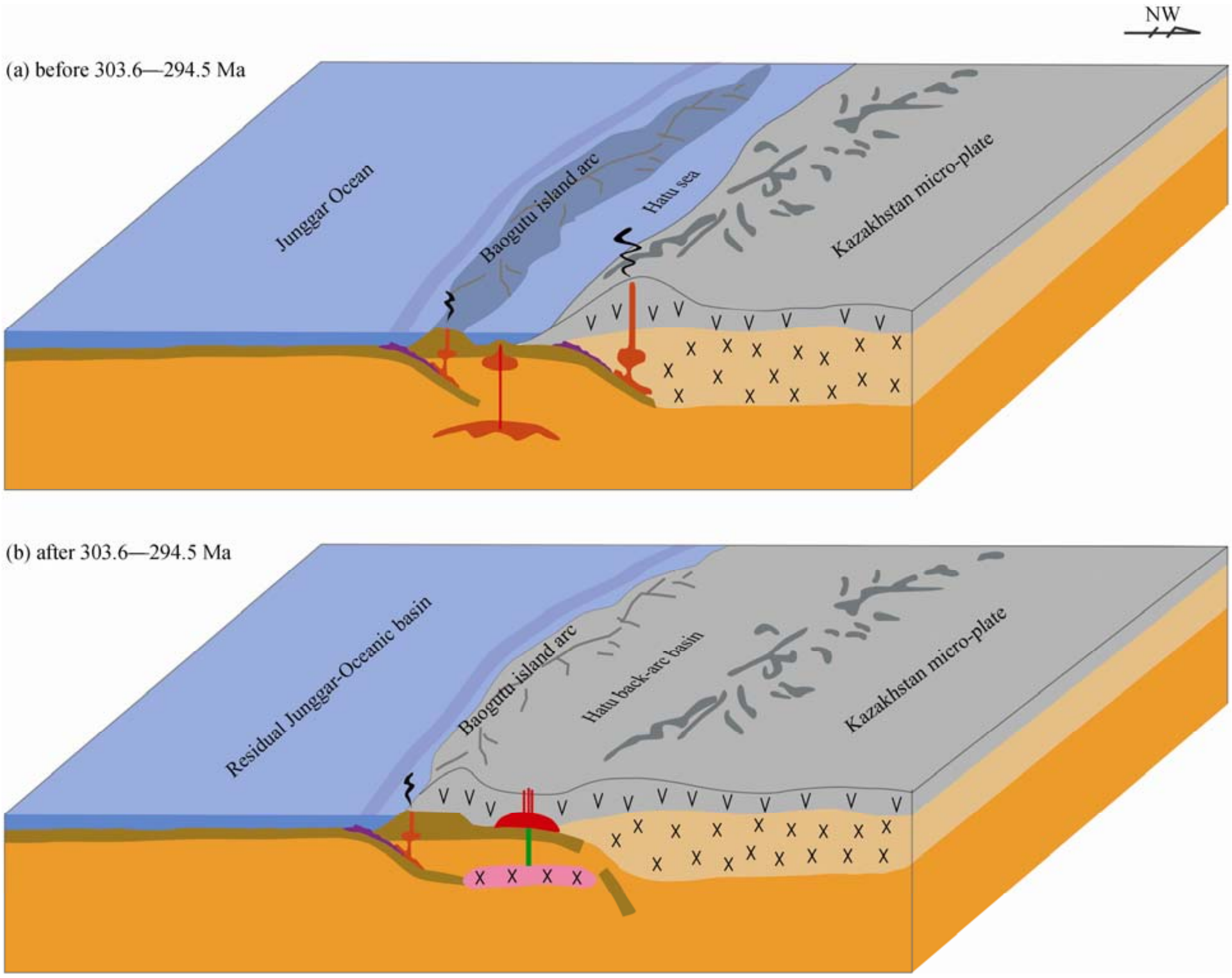

Fig. 14. Schematic illustrations displaying the tectonic settings for the West Junggar area before Late Carboniferous–Early Permian (a) and after Late Carboniferous–Early Permian (b).

2011) all have national geological parks that are well-known for their exposures of columnar jointed rhyolite, which could reflect the ocean-continent transition environment that facilitated the columnar jointed rhyolite.

By comparing our results to rhyolites from intracontinental areas such as eastern China and Japan, or marginal seas and island arcs that are close to continental margins, combined with the unique columnar joints of the rhyolite from the West Pacific tectonic transition zone, we suggest that the Late Carboniferous–Early Permian columnar jointed rhyolite from the West Junggar is comparable to concurrent rhyolite from Balkhash, Kazakhstan, which also represents an ocean-continent transitional tectonic environment during the closure of the Paleo–Asian Ocean. According to its present location, the southeastern side of the rhyolite area is affected by subduction of an oceanic plate (Junggar Ocean) beneath the Kazakhstan micro-plate (characterized by the development of island arc and accretionary wedge). Therefore, the area of origin for the rhyolite is the continental margin of the Kazakhstan micro-plate (Fig. 14).

Considering what is currently known about columnar jointed rhyolite, the Late Carboniferous–Early Permian columnar jointed rhyolite of West Junggar in the western CAOB shows characteristics of earlier formation and complete preservation, of which the formation age is far earlier than exposures in eastern China. This may be one of the oldest columnar jointed rhyolite preserved worldwide, which is of tectonic significance and scenery value. It is worth investigating further.

7 Conclusions

(1) Zircon U-Pb dating of the columnar jointed rhyolite suggests an age of 303.6–294.5 Ma, which belongs to Late Carboniferous–Early Permian.

(2) Petrogeochemical characteristics show that the rhyolite reveals a same magmatic origin as the Miaoergou batholith, which occurred in a post-orogenic extensional tectonic environment.

(3) Petrological, chronological and geochemical characteristics of the columnar jointed rhyolite suggest that the West Junggar area lived in an ocean-continent transitional tectonic environment, in which an oceanic subduction environment changed into an intracontinental environment during the Late Carboniferous–Early Permian.

Acknowledgements

We are very grateful to Dr. Wang Zengzhen and Chen Hongxu for their helpful discussions. This work was supported by the China Geological Survey (grant numbers DD20160083 and DD20160344-05), the National Key Research and Development Program of China (grant numbers 2018YFC0603701) and Fundamental Research Funds for Central Public Welfare Research Institutes (grant numbers CAGS-YWF201706).

Manuscript received Oct. 20, 2018
accepted Jan. 10, 2019
associate EIC HAO Ziguo
edited by LIU Lian

References

Ai, J., Lü, X.B., Li, Z.W., and Wu, Y.L., 2018. A super-large graphite deposit discovered in granite rocks at Huangyangshan, Xinjiang, China. *China Geology*, 1(1):164–166.

Belousova, E.A., Griffin, W.L., O'Reilly, S., and Fisher, N.I., 2002. Igneous zircon: Trace element composition as an indicator of source rock type. *Contibutions to Mineralogy and Petrology*, 143(5): 602–622.

Buslov, M.M., Fujiwara, Y., Iwata, K., and Semakov, N.N., 2004. Late Paleozoic–Early Mesozoic Geodynamics of Central Asia.*Gondwana Research*, 7(3): 791–808.

Chen, J.F., Han, B.F., and Zhang, L., 2010. Geochemistry, Sr-Nd isotopes and tectonic implications of two generations of Late Paleozoic plutons in northern West Junggar, Northwest China. *Acta Petrologica Sinica*, 26(8): 2317–2335 (in Chinese with English abstract).

Chen, X.H., Chen, Z.L., and Yang, N., 2009. Study on Regional Mineralizations and Ore-field Structures: Building of Mineralizing Tectonic Systems. *Journal of Geomechanics*, 15 (1): 1–19 (in Chinese with English abstract).

Chen, X.H., Yang, N., Ye, B.Y., Wang, Z.H., and Chen, Z.L., 2011. Tectonic System and its Control on Metallogenesis in Western Junggar as Part of the Central Asia Multi-Core Metallogenic System. *Geotectonica Et Metallogenia*, 35(3): 325–338 (in Chinese with English abstract).

Chen, X.H., Seitmuratova, E., Wang, Z.H., Chen, Z.L., Han, S.Q., Li, Y., Yang, Y., Ye, B.Y., and Shi, W., 2014. SHRIMP U-Pb and Ar-Ar geochronology of major porphyry and skarn Cu deposits in the Balkhash Metallogenic Belt, Central Asia, and geological implications. *Journal of Asian Earth Sciences*, 79(2): 723–740.

Chen, X.H., Nie, L.S., Ding, W.C., Wang, X.Q., Wang, Z.H., and Ye, B.Y., 2015. The relationship between strike-slip tectonic system and geochemical anomalies in the West Junggar, northwestern China and its implication for mineral exploration. *Acta Petrologica Sinica*, 31(2): 371–387 (in Chinese with English abstract).

Chen, X.H., Wang, Z.H., Chen, Z.L., Seitmuratova, E., Han, S.Q., Zhou, Q., and Ye, B.Y., 2015.SHRIMP U-Pb, Ar-Ar and fission-track geochronology of W-Mo deposits in the Balkhash Metallogenic Belt (Kazakhstan): Central Asia, and the geological implications. *Journal of Asian Earth Sciences*, 110(2): 19–32.

Eby, G.N., 1992. Chemical Subdivision of the A-type Granitoids: Petrogenetic and Tectonic Implications. *Geology*, 20(7): 641–644.

Fang, S.M., Li, J.F., NG, S.L., and Guo, X., 2011. Large six-party columnar joints of acidic volcanic rocks and its geological causes and significance in Hong Kong China. *Marine Sciences*, 35(5): 89–94 (in Chinese with English abstract).

Feng, Y., Coleman, R.G., Tilton, G., andXiao, X., 1989. Tectonic evolution of the West Junggar region, Xinjiang, China. *Tectonics*, 8(4): 729–752.

Frost, B.R., Barnes, C.G., Collins, W.J., Arculus, R.J., Ellis, D.J., and Frost, C.D., 2001. A geochemical classification for granitic rocks. *Journal of Petrology*, 42(11): 2033–2048.

Geng, H.Y., Sun, M., Yuan, C., Zhao, G.C., and Xiao, W.J., 2011. Geochemical and geochronological study of Early Carboniferous volcanic rocks from the West Junggar: Petrogeneses and tectonic implications. *Journal of Asian Earth Sciences*, 42(5): 854–866.

Han, B.F., Ji, J.Q., Song, B., Chen, L.H., and Zhang, L., 2006. Late Paleozoic vertical growth of continental crust around the Junggar Basin, Xinjiang, China (Part I): Timing of post-collisional plutonism. *Acta Petrologica Sinica*, 22(5): 1077–1086 (in Chinese with English abstract).

Han, B.F., Guo, Z.J., Zhang, Z.C., Zhang, L., Chen, J.F., and Song, B., 2010. Age, geochemistry, and tectonic implications of a Late Paleozoic stitching pluton in the North Tian Shan suture zone, western China. *Geological Society of America Bulletin*, 122(3): 627–640.

Hoskin, P.W.O., and Black, L.P., 2000. Metamorphic zircon formation by soild-state recrystallization of prolith igneous zircon. *Journal of Metamorphic Geology*, 18(4): 423–439.

Hu, S.X., 1992. Ponderation on problems about evolution of Mesozoic–Cenozoic Tectono–Magmatism of active continental margin in east china. *Earth Science Journal of China University of Geosciences*, S1: 40–46 (in Chinese with English abstract).

Huang, P.H., Chen, X.H., Wang, Z.H., Ye, B.Y., Li, X.Z., and Yang, Y., 2016. Late Paleozoic Granitic Magmatism in West Junggar Metallogenic Belt (Xinjiang), Central Asia, and its Tectonic Implication. *Geotectonica Et Metallogenia*, 40(1): 145–160 (in Chinese with English abstract).

Jahn, B. M., 2004. The Central Asian Orogenic Belt and growth of the continental crust in the phanerozoic. *Geological Society London Special Publications*, 226(1): 73–100.

Jin, S., Zhang, Z.Y., Rong, G.L., Liu, X.Y., Li, Y.H., Zhang, H.W., and Bi, L., 2015. Geochemical characteristics, zircon U–Pb age, and Hf isotopes of Yushenkala pluton in western Junggar, Xinjiang: Constraint on the closure of Paleo–Asian Ocean. *Geology in China*, (3): 494–508 (in Chinese with English abstract).

Kouzi, O.,andKazunori, W., 1983. the Aso Caldera. *The Earth Monthly*, 5(1): 73–82.

Laurent-Charvet, S., Charvet, J., Shu, L., Ma, R. and Lu, H., 2002. Paleozoic late collisional strikeslip deformations in Tianshan and Altay, Eastern Xinjiang, NW China. *Terra Nova*, 14(4): 249–256.

Li, D., He, D.F., Lian, Y.C., Lu, Y., and Yi, Z.J., 2017a. Structural evolution and Late Carboniferous magmatism of the Zhongguai arc in the western Junggar Basin, Northwest China: implications for tectonic evolution of the Junggar Ocean. *International Geology Review*, 59(10): 1234–1255.

Li, G.Y., Li, Y.J., Wang, X.C., Yang, G.X., Wang, R., Xiang, K.P., Liu, J., and Tong, L.L., 2017b. Identifying Late Carboniferous sanukitoids in Hala'alate Mountain, Northwest China: new constraint on the closing time of remnant ocean basin in West Junggar. *International Geology Review*, 59(9): 1116–1130.

Li, J.L., Wang, P.J., Zheng, C.Q., Tang, H.F., Wu, Y.X. and Bian, W.H., 2007. Characteristics and Genesis of Rhyolite with Columnar Joints from the Yingcheng Formation in Southeastern Uplift of the Songliao Basin. *Journal of Jilin University* (Earth Science Edition), 37(6): 1131–1138 (in Chinese with English abstract).

Li, J.Y., Chen, X.H., Wang, Z.H., Chen, W., Li, C., and Huang, P.H., 2017c. Late Palaeozoic mineralization and tectonic evolution of the West Junggar metallogenic belt, Central Asia: constraints from Re–Os and $^{40}Ar/^{39}Ar$ geochronology. *International Geology Review*, 59(9): 1131–1153.

Li, M., Zhou, S.H., Hu, Q.W., and Tian, P.R., 2007. Knowledge of porphyry Cu (Mo) ore belts in the Central Asian Metallogenic Domain and their establishment. *Geology in China*, 34(5): 870–877 (in Chinese with English abstract).

Li, W., Hu, J.M., and Qu, H.J., 2010. Fission Track Analysis of Junggar Basin Peripheral Orogen and Its Geological Significance. *Acta Geologica Sinica*, 84(2): 171–182 (in Chinese with English abstract).

Li, Y.J., Li, G.Y., Kang, L., He, X.G., Zhang, H.W., and Wang, J.N., 2013. Evidence of zircon U-Pb geochronology for magma mixing of Xiaerpu granite in West Junggar. *Acta Petrologica Sinica*, 29(9): 3023–3030 (in Chinese with English abstract).

Liu, G., She, J.Z., Yang, W.L., Wang, Q.J., Jia, J., and Di, X.C., 2018. Zircon U–Pb chronology and geochemistry of the Kalagang Formation volcanic rocks in Bayindala area,West Junggar, and their geological significance. *Geology in China*, 45(6): 1241–1250 (in Chinese with English abstract).

Liu, X.J., Xu, J.F., Wang, S.Q., Hou, Q.Y., Bai, Z.H., and Lei, M., 2009. Geochemistry and dating of E-MORB type mafic rocks from Dalabute ophiolite in West Junggar, Xinjiang and geological implications. *Acta Petrologica Sinica*, 25(6): 1373–1389 (in Chinese with English abstract).

Liu, Y.S., Hu, Z.C., Gao, S., Günther, D., Xu, J., Gao, C.G., and Chen, H.H., 2008. In *situ* analysis of major and trace elements of anhydrous minerals by LA-ICP-MS without applying an internal standard. *Chemical Geology*, 257(1): 34-43.

Ma, X.P., Zhang, M.Q., Zong, P., Zhang, Y.B., and Lv, D., 2017. Temporal and Spatial Distribution of the Late Devonian (Famennian) Strata in the Northwestern Border of the Junggar Basin, Xinjiang, Northwestern China. *Acta Geologica Sinica* (English edition), 91(4): 1413–1437.

Maniar, P.D., and Piccoli, P.M., 1989. Tectonic discrimination of granitoids. *Geological Society of America Bulletin*, 101(5): 635–643.

Middlemost, E.A.K., 1985. Magmas and Magmatic Rocks. *London: Longman*, 1–266.

Middlemost, E.A.K., 1994. Naming materials in the magma/ igneous rock system. *Earth Science Reviews*, 37(3-4): 215–224.

Miyoshi, M., Shibata, T., Yoshikawa, M., Sano, T., Shinmura, T., and Hasenaka, T., 2011. Genetic relationship between post -caldera and caldera-forming magmas from Aso volcano, SW Japan: Constraints from Sr isotope and trace element compositions. *Journal of Mineralogical and Petrological Sciences*, 106(2): 114–119.

Nakada, S., and Kamata, H., 1991. Temporal change in chemistry of magma source under Central Kyushu, Southwest Japan: progressive contamination of mantle wedge. *Bulletin of Volcanology*, 53(3): 182–194.

Pearce, J.A., Harris, N.B.W., and Tindle, A.G., 1984. Trace Element Discrimination Diagrams for the Tectonic Interpretation of Granitic Rocks. *Journal of Petrology*, 25(4): 956–983.

Pearce, J.A., 1996. Sources and settings of granitic rocks. *Episodes*,19(4): 120–125.

Rickwood, P.C., 1989. Boundary lines within petrologic diagrams which use oxides of major and minor elements. *Lithos*, 22(4): 247–263.

Sengör, A.M.C., Natal'in, B.A., and Burtman, V.S., 1993. Evolution of the Altaid tectonic collage and Paleozoic crustal growth in Asia. *Nature*, 364(6435): 299–307.

Shen, P., Shen, Y.C., Pan, H.D., Li, X.H., Dong, L.H., Wang, J.B., Zhu, H.P., Dai, H.W., and Guan, W.N., 2012. Geochronology and isotope geochemistry of the Baogutu porphyry copper deposit in the West Junggar region, Xinjiang, China. *Journal of Asian Earth Sciences*, 49(3): 99–115.

Shen, P., Pan, H.D., Xiao, W.J., Chen, X.H., Seitmuratova, E., and Shen, Y.C., 2013a.Two geodynamic–metallogenic events in the Balkhash (Kazakhstan) and the West Junggar (China): Carboniferous porphyry Cu and Permian greisen W–Mo mineralization. *International Geology Review*, 55(13): 1660–1687.

Shen, P., Pan, H.D., Xiao, W.J., Li, X.H., Dai, H.W., and Zhu, H.P., 2013b. Early Carboniferous intra-oceanic arc and back-arc basin system in the West Junggar, NW China. *International Geology Review*, 55(16): 1991–2007.

Song, H.X., Liu, Y.L., Qu, W.J., Song, B., Zhang, R., and Cheng, Y., 2007. Geological Characters of Baogutu Porphyry Copper Deposit in Xinjiang, NW China. *Acta Petrologica Sinica*, 23 (8): 1981–1988 (in Chinese with English abstract).

Su, Y.P., Tang, H.F., Hou, G.S., and Liu, C.Q., 2006. Geochemistry of aluminous A-type granites along Darabut tectonic belt in West Junggar, Xinjiang. *Geochimica*, 35(1): 55–67 (in Chinese with English abstract).

Sun, S.S., and McDonough, W., 1989. Chemical and isotopic systematics of oceanic basalts: implications for mantle composition and processes. *Geological Society London Special Publications*, 42(1): 313–345.

Sun, T., Qian, Z.Z., Thakurta, J., Yang, S.H., Xu, G., Duan, J., Gao, B., and Wang, J., 2018. Geochemical and Petrological Studies on the Early Carboniferous Sidingheishan Mafic–Ultramafic I intrusion in the Southern Margin of the Central Asian Orogenic Belt, NW China. *Acta Geologica Sinica* (English edition), 92(3): 952–971.

Tang, G.J., Wang, Q., Zhao, Z.H., Wyman, D.A., Chen, H.H., Jia, X.H., and Jiang, Z.Q., 2009. Geochronology and

Geochemistry of the Ore–Bearing Porphyries in the Baogutu Area (Western Junggar): Petrogenesis and Their Implications for Tectonics and Cu–Au Mineralization. *Earth Science-Journal of China University of Geosciences*, 34(1): 56–74 (in Chinese with English abstract).
Tang, G.J., Wang, Q., Wyman, D.A., Li, Z.X., Zhao, Z.H., Jia, X.H., and Jiang, Z.Q., 2010a. Ridge subduction and crustal growth in the Central Asian Orogenic Belt: Evidence from Late Carboniferous adakites and high-Mg diorites in the West Junggar region, northern Xinjiang (west China). *Chemical Geology*, 277(3): 281–300.
Tang, G.J., Wang, Q., Wyman, D.A., Sun, M., Li, Z.X., Zhao, Z.H., and Jiang, Z.Q., 2010b. Geochronology and geochemistry of Late Paleozoic magmatic rocks in the Lamasu–Dabate area, northwestern Tianshan (west China): Evidence for a tectonic transition from arc to post-collisional setting. *Lithos*, 119(3): 393–411.
Tao, H.F., Wang, Q.C., Yang, X.F., and Jiang, L., 2013. Provenance and tectonic setting of Late Carboniferous clastic rocks in West Junggar, Xinjiang, China: A case from the Hala–alat Mountains. *Journal of Asian Earth Sciences*, 64: 210–222.
Whalen, J.B., Currie, K.L., and Chappell, B.W., 1987. A-type granites: Geochemical characteristics, discrimination and petrogenesis. *Contributions to Mineralogy and Petrology*, 95 (4): 407–419.
Windley, B.F., Alexeiev, D.V., Xiao, W., Kröner, A., and Badarch, G., 2007. Tectonic models for accretion of the Central Asian Orogenic Belt. *Journal of the Geological Society of London*, 164(12): 31–47.
Xiao, W.J., Han, C.M., Yuan, C., Chen, H.L., Sun, M., Lin, S.F., Li, Z.L., Mao, Q.G., Zhang, J.E., Sun, S., and Li, J.L., 2006. Unique Carboniferous–Permian tectonic–metallogenic framework of northern Xinjiang (NW China): Constraints for the tectonics of the southern Paleoasain Domain. *Acta PetrologicaSinica*, 22(5): 1062–1076 (in Chinese with English abstract).
Xiao, W.J., Han, C.M., Yuan, C., Sun, M., Lin, S.F., Chen, H.L., Li, Z. L., Li, J.L., and Sun, S., 2008. Middle Cambrian to Permian subduction-related accretionary orogenesis of Northern Xinjiang, NW China: Implications for the tectonic evolution of central Asia. *Journal of Asian Earth Sciences*, 32 (2): 102–117.
Xiao, W.J., and Kusky, T., 2009. Geodynamic processes and metallogenesis of the Central Asian and related orogenic belts: Introduction. *Gondwana Research*, 16(2): 167–169.
Xiao, W.J., Li, S.Z., Santosh, M., and Jahn, B.M., 2012. Orogenic belts in Central Asia: Correlations and connections. *Journal of Asian Earth Sciences*, 49(3): 1–6.
Xing, G.F., Tao, K.Y., Yang, Z.L., Zhao, Y., and Xu, N.Z.,1999. The Summarizing about the Reasons Causing the Formation of Mesozoic Igneous Rock in Southeast China Near the Reason. *The Bulletin of Mineralogy, Petrology and Geochemistry*, 18(3): 189–193 (in Chines).
Xing, G.F., Ng, Y.C.Y., Tao, K.Y., Ng, S.L., Chen, R., Jiang, Y., Li, L.M., and Yu, M.G., 2011. Petrological study of High Island Formation volcanic columns in the Hong Kong National Geopark. *Geology in China*,38: 1080–1093 (in Chinese with English abstract).
Xu, S.N., 1995. Dsicovery of Columnar Joint Structure of Mesozolc Acidic Volcanic Rocks in ZheJiang Province and Its Geological Siginificance. *Acta Petrologica Sinca*,11(3): 325–332 (in Chinese with English abstract).
Yakubchuk, A., 2004. Architecture and mineral deposit settings of the Altaid orogenic collage: A revised model. *Journal of Asian Earth Sciences*, 23(5): 761–779.
Yakubchuk, A., 2008. Re-deciphering the tectonic jigsaw puzzle of northern Eurasia. *Journal of Asian Earth Sciences*, 32(2): 82–101.
Yang, F.Q., Mao, J.W., Pirajno, F., Yan, S.H., Liu, G.R., Zhou, G., Zhang, Z.X., Liu, F., Geng, X.X., and Guo, C.L., 2012. A review of the geological characteristics and geodynamic setting of Late Paleozoic porphyry copper deposits in the Junggar region, Xinjiang Uygur Autonomous Region, Northwest China. *Journal of Asian Earth Sciences*, 49(3): 80-98.
Yang, Y., Chen, X.H., Chen, Z.L., Han, S.Q., Seitmuratova, E., Wang, Z.H., Shi, W., and Ye, B.Y., 2015. The latest granitic intrusive magmatism and thermal evolution in the Late Paleozoic Balkhash Metallogenic Belt (Kazakhstan), Central Asia. *Acta Petrologica Sinica*, 31(2): 304–314 (in Chinese with English abstract).
Yin, J.Y., Chen, W., Xiao, W.J., Yuan, C., Sun, M., and Cai, K.D., 2018. Petrogenesis and tectonic implications of Early Devonian mafic dike-granite association in the northern West Junggar, NW China. *International Geology Review*, 60(4): 87–100.
Yu, M.J., Wang, J.B., Mao, Q.G., Fang, T.H., and Zhang, R., 2018. Ore–forming Fluid and Mineral Source of the Hongshi Copper Deposit in the Kalatage Area, East Tianshan, Xinjiang, NW China. *Acta GeologicaSinica* (English Edition), 92(5): 1769–1783.
Zhan, Y., Hou, G.T., Hari, K.R., andShu, W.L., 2015. Geochemical and isotopic constraints on the evolution of Late Paleozoic dyke swarms in West Junggar, Xinjiang, China. *Journal of Asian Earth Sciences*, 113: 126–136.
Zhang, D., Lu, Y.M., Pan, A.J., Chao, Y.Y., Fan, J.J., and Zhang, Y.J., 2011. Two Types of Calcium Alkaline Granite and Their Tectonic–Metallogenic Significance in North Margin of Eastern Junggar. *Northwestern Geology*, 44(2): 51–71 (in Chinese with English abstract).
Zhang, P., Wang, G.C., Li, Y.T., Zhang, S.Y., Peng, C., Zhao, H.W., and Zha, Y.H., 2017. Emplacement Mechanism of the Akebasitao Pluton: Implications for Regional Tectonic Evolution of West Junggar, NW China. *Acta Geologica Sinica* (English edition), 91(3): 857–874.
Zhang, Q., Ran, H. and Li, C.D., 2012. A-type Granite: What is the Essence?. *Acta Petrologica ET Mineralogica*, 31(4): 626–631 (in Chinese with English abstract).
Zhang, X., 2001. The geologic features of the Early Cretaceous rhyolite in the Shanmen area, Siping, Jilin province. *Jilin Geolgy*, 20(3): 30–34 (in Chinese with English abstract).
Zhao, L., and He, G.Q., 2013. Tectonic entities connection between West Junggar (NW China) and East Kazakhstan. *Journal of Asian Earth Sciences*, 72(4): 25–32.
Zhou, T.F., Yuan, F., Fan, Y., Zhang. D.Y., Cooke, D., and Zhao, G.C., 2008. Granites in the Sawuer region of the West Junggar, Xinjiang Province, China: Geochronological and geochemical characteristics and their geodynamic significance. *Lithos*, 106(3): 191–206.
Zhu, Y.F., Chen, B., Xu, X., Qiu, T., and An, F., 2013. A new geological map of the West Junggar, north Xinjiang (NW China): Implications for Paleoenvironmental reconstruction. *Episodes*, 36(3): 205–220.

About the first author

XU Shenglin, male, born in 1990 in Yantai City, Shandong Province; doctoral candidate; attending China University of Geosciences (Beijing) & Chinese Academy of Geological Sciences; Structural Geology majors; engages in researchon tectonics and geochemistry.E-mail: xushenglindizhi@163.com. Phone: 010-68999902, 13041119238.

About the corresponding author

CHEN Xuanhua, male, born in 1967; Researcher of Chinese Academy of Geological Sciences; doctoral advisor; graduated from Peking University; He is now interested in the study on deep earth exploration. Email: xhchen@cags.ac.cn; phone: 010-68999902, 15801123149.